Validation of US3D for Capsule Aerodynamics using 05-CA Wind Tunnel Test Data

Alan M. Schwing

Department of Aerospace Engineering and Mechanics

University of Minnesota, Minneapolis, MN, 55455

Several comparisons of computational fluid dynamics to wind tunnel test data are shown for the purpose of code validation. The wind tunnel test, 05-CA, uses a 7.66% model of NASA's Multi-Purpose Crew Vehicle in the 11-foot test section of the Ames Unitary Plan Wind tunnel. A variety of freestream conditions over four Mach numbers and three angles of attack are considered. Test data comparisons include time-averaged integrated forces and moments, time-averaged static pressure ports on the surface, and Strouhal Number. The applicability of the US3D code to subsonic and transonic flow over a bluff body is assessed on a comprehensive data set. With close comparison, this work validates US3D for highly separated flows similar to those examined here.

I. Introduction

NASA is currently working on developing a new Multi-Purpose Crew Vehicle (MPCV) - formerly the Crew Exploration Vehicle (CEV). The MPCV will support manned missions to low earth orbit, lunar orbit, and destinations further afield. It is slated as the replacement to the recently retired Space Shuttle and will act as the workhorse for NASA's manned missions in the future.

During two phases of flight (abort and re-entry), the manned component of the MPCV is a crew capsule that strongly resembles the Apollo Command Module (CM) used in the 1960's. Figure 1 shows an isometric view of the new CM and a definition of major parameters that will be used in this paper. There are stringent requirements on the performance of this vehicle and a slightly modified geometry. While similar to the Apollo CM, this necessitates an independent characterization of the aerodynamics - the integrated loads experienced by a vehicle during flight. For these reasons, the Apollo aerodynamic models, while significant in depth of test and flight data, are insufficient to rely upon complete for the design of the MPCV CM.

In the development of this new vehicle, computational fluid dynamics (CFD) and wind tunnel testing have been used significantly to assess its performance. Wind tunnel tests are important because they exactly represent the flow - the physics are real. While the physics are real, they are not completely predictive of how a full-scale vehicle model might perform in flight. They explore aerodynamic effects on a scaled model at a limited set of flight conditions, but they do allow precise measurement of quantities that are of interest to design engineers. Data from wind tunnel tests is also used to validate CFD codes used in development. By validating a CFD code at the known conditions in the wind tunnel, engineers obtain greater confidence in the tools. This allows them to run additional CFD cases are conditions that are too challenging or expensive (or impossible) to obtain using ground test facilities.

A significant challenge for the MPCV program is achieving convincing CFD comparisons to wind tunnel test data for aerodynamics at subsonic, transonic, and low supersonic conditions. Several CFD codes have been used in these comparisons and have had mixed success. Poor comparisons are not entirely surprising due to the complexity of the flowfield and the sensitivity of the aerodynamics to modeled and insufficiently realized physics. For the CM, there is a significantly separated wake dominated by turbulent eddies and dynamic flow structures. The majority of past work has used Reynolds-Averaged Navier-Stokes (RANS) turbulence models. This paper will investigate using low-dissipation, high-order Detached Eddy Simulations

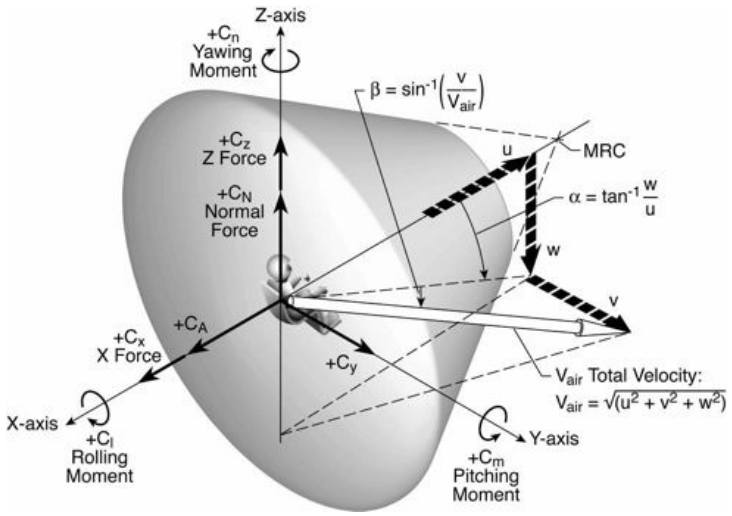

Figure 1. Isometric view of MPCV Crew Module and definition of coordinate axes and major flow parameters.

(DES) to more accurately match the wind tunnel test data and provide an avenue for improved numerical prediction of vehicle performance.

This paper will also serve to assess current practices with US3D on bluff body shapes of this nature. US3D is a leading-edge CFD code currently under development at the University of Minnesota. It has a robust group of researchers working to active novel and highly-accurate methods for capturing delicate flow phenomena and resolving detailed flow interactions. Recently, there has been a desire to begin using US3D on capsule shapes and this work will be helpful in understanding the reliability of its results.

II. Wind Tunnel Test

A major wind tunnel test performed in support of MPCV development was conducted at NASA Ames Research Center (ARC) in 2006. This test, 05-CA,[1] used three models across two wind tunnel test sections of the Unitary Plan Wind Tunnel in order to collect data at a large range of Mach and Reynolds numbers. Of importance to this work is the data collected in the 11-foot transonic test section. The work in the 11-foot comprised of a 7.66% scale model of the MPCV CM at Mach numbers from 0.5 to 1.4 and angles of attack (α) from 140° to 170° at Reynolds numbers (based on CM diameter) from 1.89E6 to 5.30E6. Figure 2 shows a vertical orientation of the sting and CM model in the 11-foot transonic test section at two orientations.

Instrumentation included in the model and balance provided a wealth of test data for validation work. In addition to a six-component balance - necessary to capture the integrated loads most important to the program - there were 168 static pressure taps distributed across the model to measure surface pressure and 11 unsteady transducers to measure high-speed pressure fluctuations to quantify wake shedding dynamics. All three data sources will be used in the comparisons below. Table 1 highlights the Mach and α pairs that will be examined computationally in this work and the run conditions for these experiments. In the subsequent discussion, for each Mach number, the angles of attack will be referred to by their nominal values: 140°, 155°, 170°.

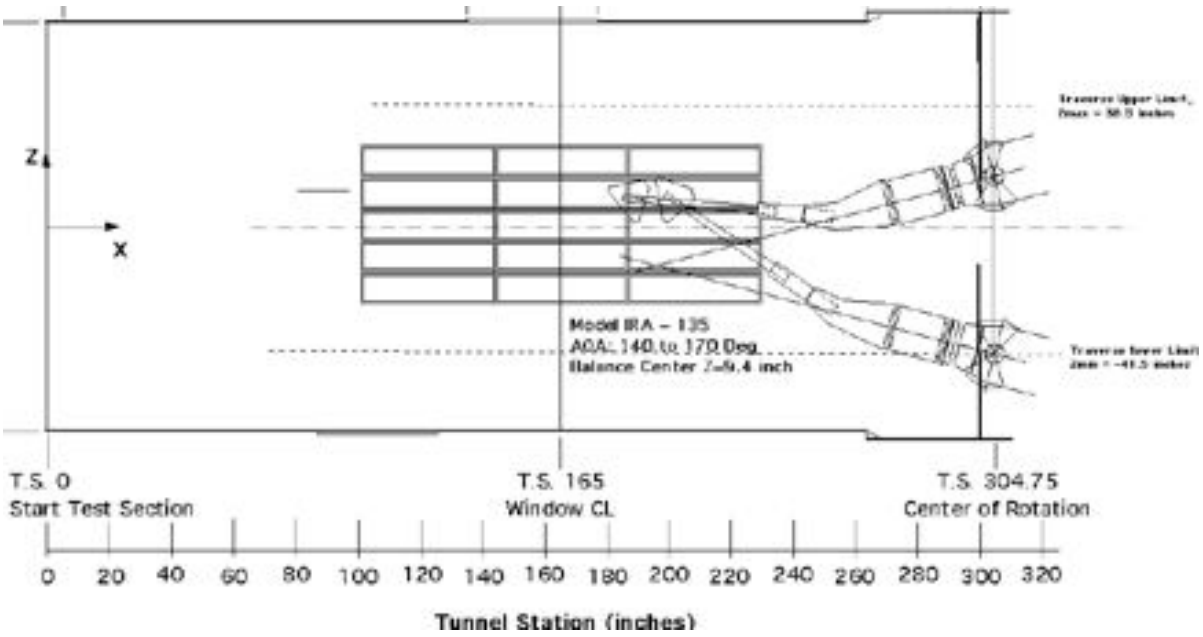

Figure 2. View of sting, model, and tunnel walls for two orientations in the 11-foot transonic test section.

Mach	Angle of Attack (α)	Angle of Sideslip (β)	RE_D	V_∞ [m/s]	ρ_∞ [kg/m^3]	T_∞ [K]
0.50	141.73°	0.11°	5.30E6	168.08	1.43960	295.61
	155.63°	0.12°	5.31E6	168.32	1.43940	281.65
	169.57°	0.10°	5.30E6	168.18	1.44050	282.15
0.95	142.32°	0.09°	5.31E6	304.48	0.73691	255.46
	154.36°	0.12°	5.30E6	303.28	0.73920	255.57
	170.48°	0.08°	5.30E6	302.99	0.74083	256.23
1.40	142.79°	0.11°	5.32E6	411.49	0.48805	222.18
	155.22°	0.13°	5.32E6	413.90	0.48176	220.64
	169.25°	0.11°	5.33E6	414.35	0.47878	219.42

Table 1. Run matrix and wind tunnel conditions examined in this analysis.

III. Computational Methodology

A. Flow Solver and Numerics

For this work, the US3D flow solver[2,3] is employed across the entire run matrix. US3D is a finite-volume, unstructured CFD code written and developed at the University of Minnesota. The code is fully parallel and was run on 192 processor for the majority of this work. It employs Steger-Warming (SW) flux vector splitting for the convective fluxes. In addition, low-dissipation, high-order numerics for the convective fluxes are also included. These Kinetic Energy Conserving (KEC) fluxes are less dissipative than unwinding (SW) and allow for smaller scale gradients on a given mesh and a broader energy spectrum.[4] Viscous fluxes in the Navier-Stokes equations use a deferred-correction approach.

US3D employs two methods for computing turbluence: the Spalart-Allmaras RANS turbulence model, and Large Eddy Simulation (LES). Computations can use the RANS model everywhere or they can use a hybrid of RANS and LES to remove some of the modeling - this hybrid is referred to as Detached Eddy Simulations (DES). DES is heavily utilized in this work as it allows for more-accurate LES in regions of the flow including turbulence - a major driver in separated flowfields similar to those examined here.

Several time advancement machines are available, both implicit and explicit. The following results used 2nd-order implicit Euler time advancement , allowing very large timesteps. For this work, the Ducros switch was used to add dissipative fluxes (SW) to the non-dissipative KEC fluxes where appropriate.[5]

B. Discretization

The quality of a CFD solution depends on the quality of the grid used in the computation. Additionally, in order to ensure time-accuracy, an appropriately small timestep is required. Several metrics are explored in order to verify that the grid and timestep used in this work are reasonable and do not contribute a significant error to these results.

1. Grid - Spatial Discretization

Figure 3 shows three views of a computational mesh used for preliminary simulations. Due to the large majority of cases being subsonic and transonic, the boundaries of the grid extend thirty CM diameters downstream and upstream of the vehicle in order to reduce their potential influence on the solution. Additionally, the point spacing increases near the extents of the grid in order to eliminate gradients near those boundaries.

Only a subset of the wind tunnel sting is modeled in the computation. The portion nearest to the model is included due to its obvious influence on the flow near the capsule. Wind tunnel walls are not modeled for two reasons:

1. Previous work performed by NASA using OVERFLOW showed a small combined effect due to the tunnel and sting.[6] For this reason, it was not deemed important enough to fully implement and validate the porous boundary condition in US3D for the 11- foot transonic tunnel.

2. With the tunnel included, a separate grid is required for each angle of attack. With the number of grid points considered in the analysis and the inability to run GirdPro to run in parallel, smoothing alone would take considerable computational time. Additionally, such grids would also require independent topologies would would also add expense and potential differences between cases. Buy using one grid for all cases, these limitations are avoided.

The grids were generated using GridPro, a multi block grid generator and smoother. GridPro uses a topological approach where grid blocks are generate and constrained to provided geometry. It uses an algebraic-elliptic smoother to turn the non-ideal topological grid blocks into a combined mesh with smoothly varying grid lines. For this analysis, the topology relied on both nested refinement and 'grid baffles' in order to resolve the wake portion of the flow and to properly align the grid with significant portions of the geometry. This results in somewhat noticeable grid shocks and singularities but it is not believed that either of these artifacts cause a reduction in agreement with the experiment.

Several different grid systems will be evaluated, each with successively more cells than the the last, in order to determine the minimum number of points necessary to resolve all significant flow features. Table 2 shows the range of grids examined for this work. Grid convergence will be measured by monitoring the

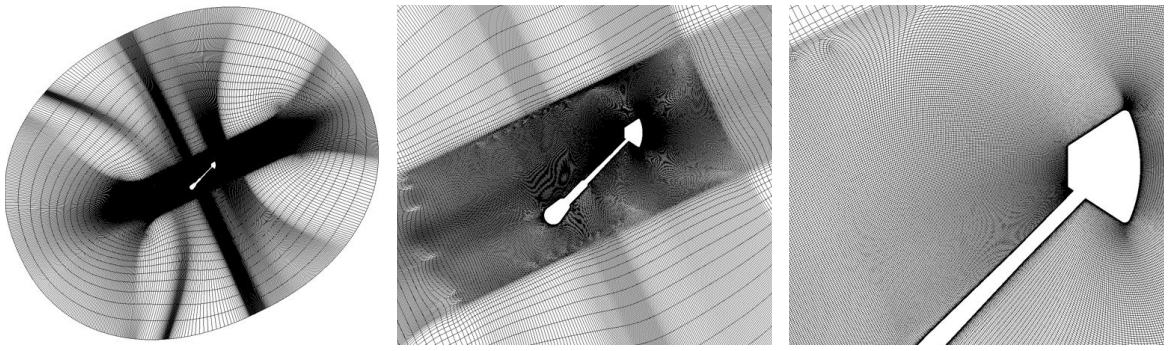

Figure 3. Three views of the grid in the pitch plane for the fine, full 3D grid.

change in significant quantities as the grid is refined: time-averaged integrated aerodynamic quantities. At the point where these quantities stop changing with refinement, the grid is considered converged and that density will be used for the entire case matrix.

Label		Number of Cells
Coarse	Symmetric	2,337,664
Medium	Symmetric	7,272,595
Fine	Symmetric	11,638,110
Medium	Full 3D	8,812,944
Fine	Full 3D	18,113,216

Table 2. Table of grid size for cases run in refinement study.

To save on computational expense and develop a feel for how sensitive these cases are to grid refinement, a symmetric case was used for the initial grid refinement. This grid was identical to a three-dimensional case, but with a symmetry plan placed along the pitch plane (Y=0 according to Fig. 1). Using those initial three runs, the grid topology was modified and expanded to three-dimensions and a more limited study was performed using grids that mimicked the surface spacing of the finest two symmetric cases. Figure 4 shows the integrated aerodynamic coefficients results from that study at $\alpha = 155°$for all Mach numbers considered.

An important note for Fig. 4 is the inclusion of error bars on the results. Those error bars will be included on all aerodynamic loads and are to put these results into perspective. The width of the bars represents changes of significance relative to the test data - results that vary on the order of these convergence tolerances are considered to be nearly indistinguishable for the purposes of comparing to data. This will be evident later in this paper when computational results are shown with the wind tunnel results.

Figure 5 shows a qualitative comparison of the flow at Mach 1.4 and α =155° with the two grid refinement levels for the 3D case. These are instantaneous snapshots of an unsteady flowfield, so discrepancies in the unsteady portions are expected. The top of each figure shows contours of Mach number while the bottom half shows the log of the density gradient magnitude. It is obvious that a greater range exists between the smaller and largest scale motions for the more refined case, but the differences are not enough to contribute greatly to the integrated loads (as indicated by the agreement in Fig. 4).

2. Timestep - Temporal Discretization

Similar to the grid convergence study, a temporal convergence study was performed. The coarse symmetric grid was run at varying timesteps to determine the integrated quantities sensitivity to the global Courant-Friedrichs-Lewy (CFL) number. Figure 6 shows temporal history of several integrated quantities for a range of CFL numbers. Starting from a developed solution, each case was advanced using the CFL number indicated in the plot. Also indicated on the plot are the convergence tolerances mentioned previously.

The significant result from the figure is that while there are noticeable deviations between the cases both in magnitude and character of the oscillations, the extend of the differences do not exceed the previously

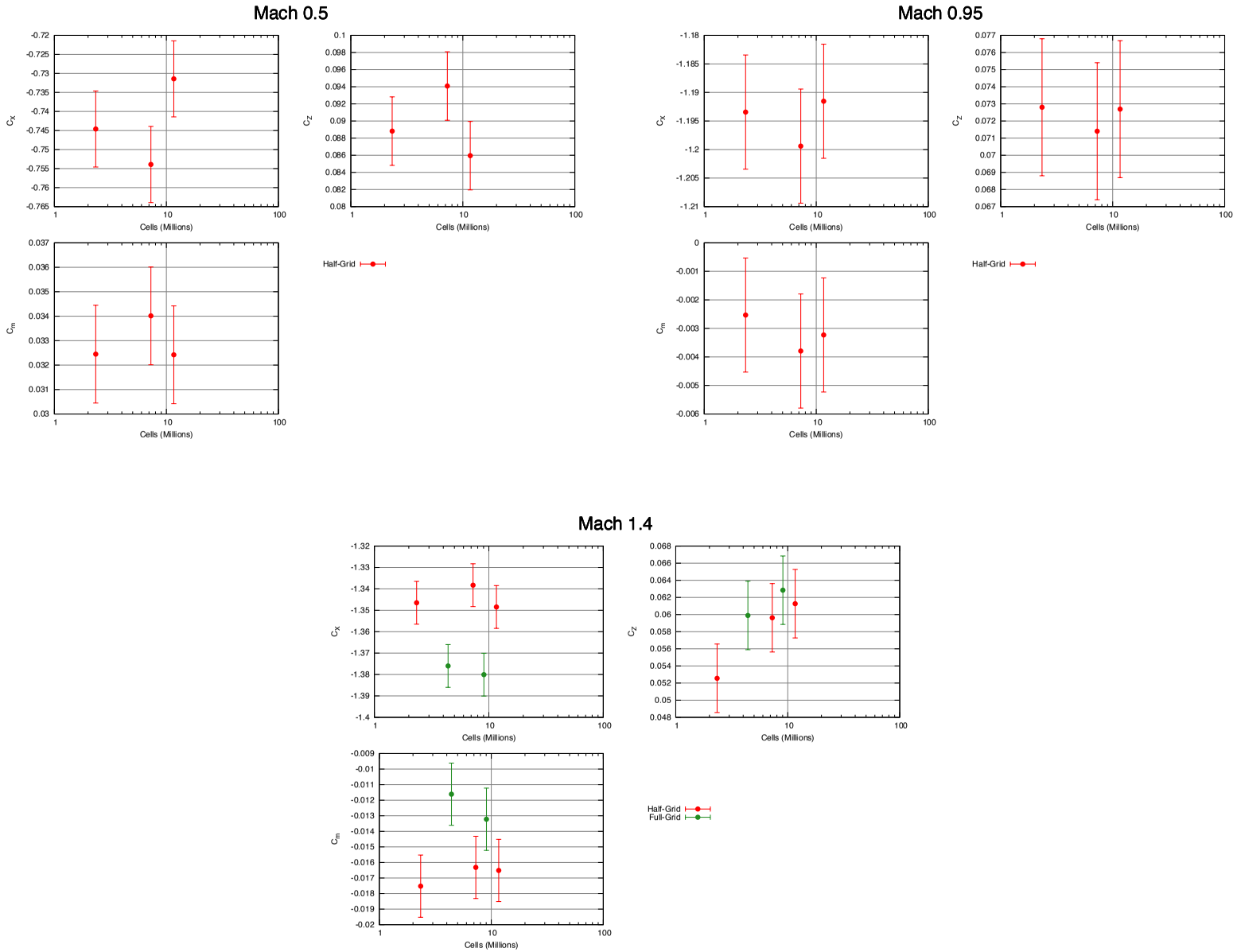

Figure 4. Grid study results for three Mach numbers all at $\alpha = 155°$. Error bars represent scale of meaningful difference. Grid cell count halved for Full-Grid.

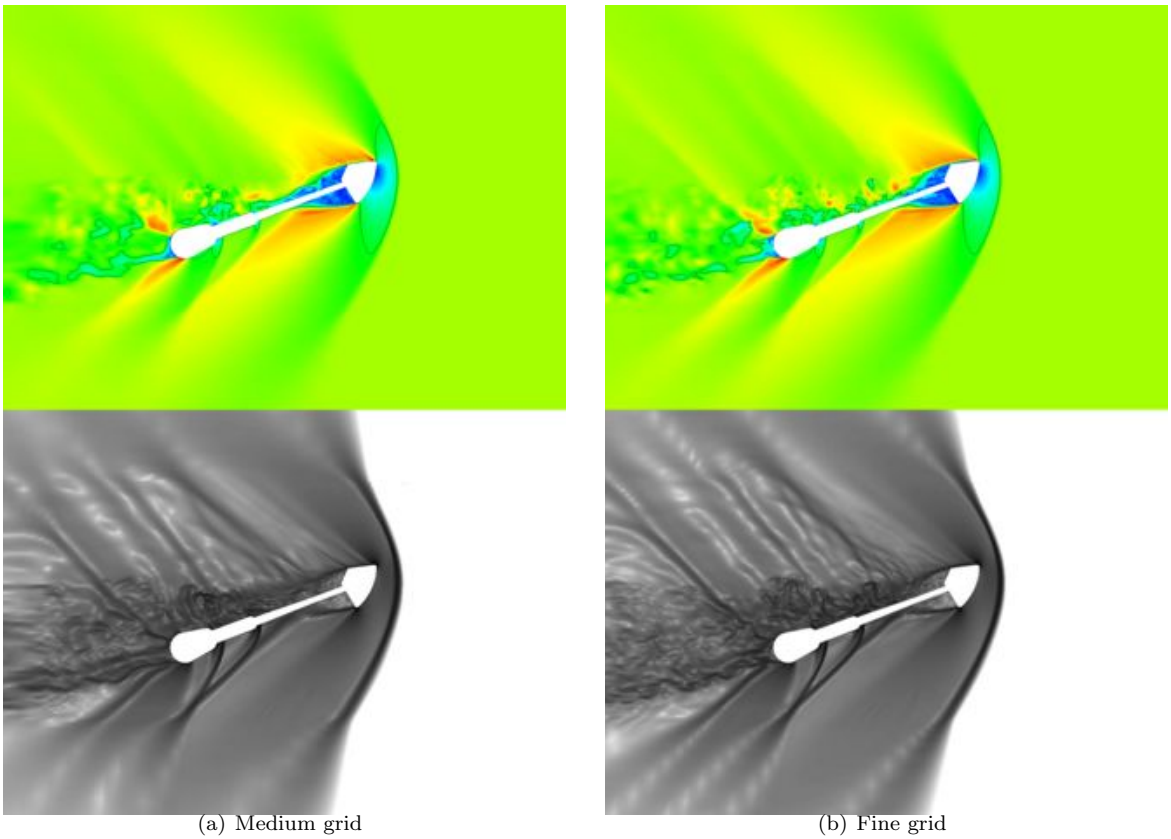

(a) Medium grid (b) Fine grid

Figure 5. Qualitative comparison of Mach number (top) and log of density-gradient magnitude (bottom) in pitch plane for 3D grids. Results are for Mach 1.4, $\alpha = 155^\circ$ with 8,812,944 cells in 'Medium', 18,113,216 cells in 'Fine'.

accepted convergence tolerances. In other words, these cases are not significantly different compared to the magnitude of the wind tunnel data that they approximate. It is worth reminding the reader that reported integrated loads are averaged over the last several thousand time steps. With that perspective, these results collapse even further and in the light of the (relatively) large convergence tolerance imply that any one of these CFL values is sufficient for subsequent analysis.

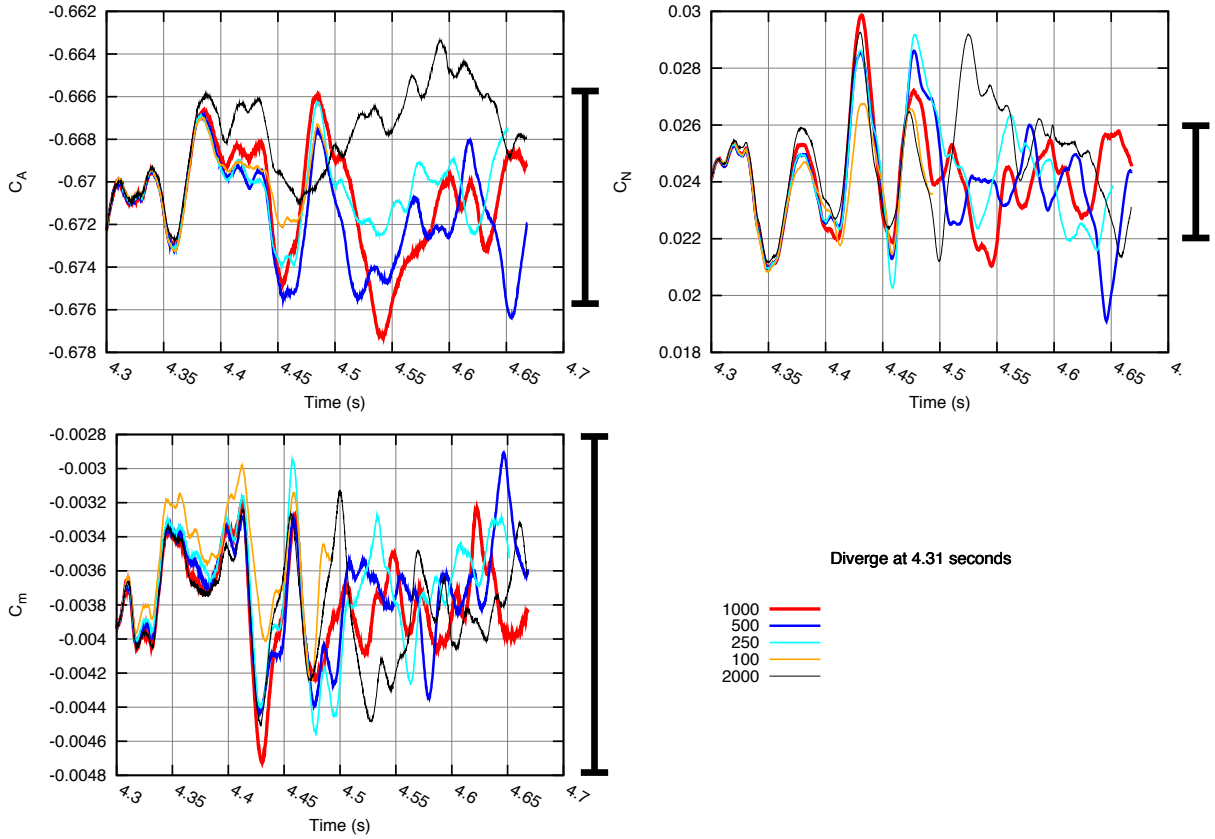

Figure 6. Integrated load histories for Mach 1.4, $\alpha = 155^\circ$ cases using a range of CFL numbers. Cases start from a common solution at t=4.31 seconds. Black bars indicate previously described convergence tolerances.

For best results, previous work with US3D has shown that a local CFL less than unity in the wake region is a necessary condition for time-accuracy. Figure 7 shows a contour of CFL in a slice through the pitch plane for the CFL of 1000 case shown previously. The vast majority of the flow field has a local CFL value less than 1. Similar analysis at Mach 0.95 and 0.5 suggested maximum CFL values of 1500 and 2000 respectively. Reducing the time step further would reduce the error in the temporal discretization, but to decrease the wall time necessary to converge solution these maximum CFL values were selected for all subsequent analysis.

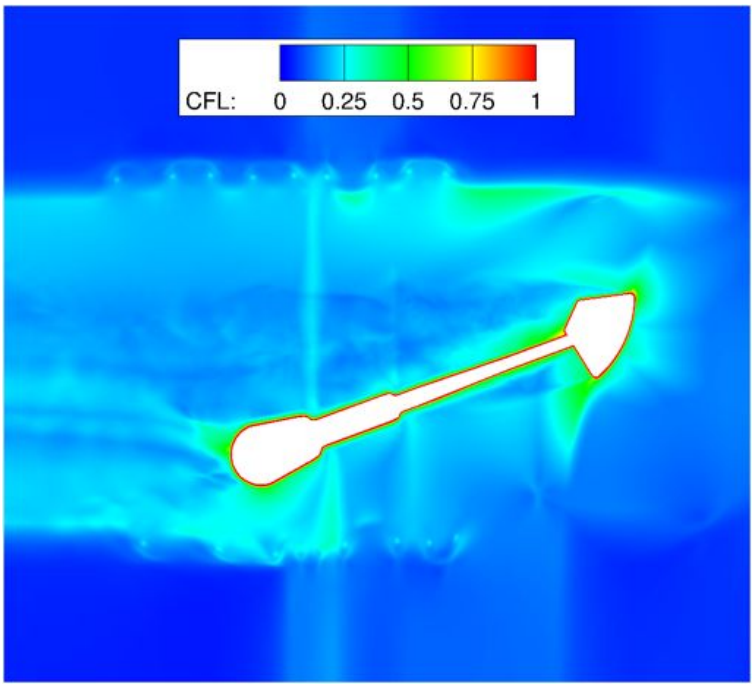

Figure 7. Local CFL in the pitch plane for a Mach 0.5 simulation in the vicinity of the body.

IV. Results

A major goal of this work was to help assess the ability of US3D at predicting the aerodynamic loads on the model capsule. In order to understand the sensitivities and requirements, three different numerical techniques are compared. The designations used later in this section and their differences are described here.

RANS-KEC These simulations used the RANS Spalart-Allmaras turbulence model throughout the entire flow field. They also include the second-order, low-dissipation kinetic energy conserving fluxes (KEC).

DES-SW These simulations use Detached Eddy Simulation (DES) to model turbulence with the Spalart-Allmaras eddy-viscosity model. For the convective fluxes, they employ the Steger-Warming fluxes. These fluxes are more dissipative than their KEC counterparts.

DES-KEC These simulations use Detached Eddy Simulation (DES) to model turbulence with the Spalart-Allmaras eddy-viscosity model. They also include the second-order, low-dissipation kinetic energy conserving fluxes (KEC). It is expected that these cases are the highest fidelity due to the low-dissipation fluxes and use of LES though out much of the flow field.

Integrated forces and moments were of primary importance to this work. Comparisons to the wind tunnel results are determined by averaging the unsteady, integrated loads from US3D over the last (approximately) 0.3 seconds of runtime CHECK AMS. For some cases, pressure port measurements are examined in order to better understand why and where discrepancies exist. This data is not examined for all cases, but a complete set of images and comparisons are presented at the end of this document for each Mach-α combination.

The integrated loads reported by the tunnel included a correction to account for the area of the sting and balance and report an expected value for a free-flight capsule. They did this by using pressure ports on the surface and inside the model. A similar procedure was included in this work. Pressure values on the backshell in the vicinity of the sting were averaged in order to estimate an effective pressure to apply for the area under the sting.

A. Mach 1.40

The supersonic case is the most steady of those examined here and is the most likely to show strong agreement between the tunnel results and the computation. Pressure on the forebody or heatshield is largest and and errors associated with the modeling of the unsteady wake (dissipation, dispersion, or turbulent quantities) will have a reduced effect due to the small size of the wake and the inability for poor prediction downstream to effect massive changes upstream.

Figure 8 shows the comparisons between the tunnel and the computation integrated aerodynamic loads. Similar figures will be shown for each subsequent Mach number. The experimental data is shown for an entire α-sweep at this condition and the numerical results are shown at the three angles of attack selected for this comparison. Error bars representing the previously described convergence tolerance are plotted for all cases, but their relative magnitudes make them hard to discern for aerodynamic coefficients whose magnitude is large. As listed on the plot, the location for the center of mass was taken to be the reference point for the pitching moment ($C_{m_{cg}}$). That non-dimensional position was at (X,Y,Z) = (0.680D, 0,- 0.045D).

Due to the unsteadiness in these problems, the surface pressure measurements were averaged over a number of iteration in order to determine mean pressure distribution on the model. The last X iterations CHECK AMS of each case were included in an ensemble average to create this mean flowfield. This method effectively converged the pressure distribution on the model backshell. For an illustration of the amount of unsteadiness this removed, refer to the contour images at the end of this document. For example, Fig. 22 shows an illustration of a very unsteady flowfield averaged over a significant time to produce more coherent, averaged structures.

All of the numerical results do a fair job of matching the data for the conditions examined here. Of the three, the RANS-KEC appears to over predict the magnitude of the drag coefficient, the majority of the error arising from the axial direction. DES-SW, over the results shown here provides the closest match to the wind tunnel data. The expectation was that DES-KEC, with its less-dissipated convective fluxes would provide the best comparison. While still competitive, it is clear that the second-order KEC fluxes are not advantageous here.

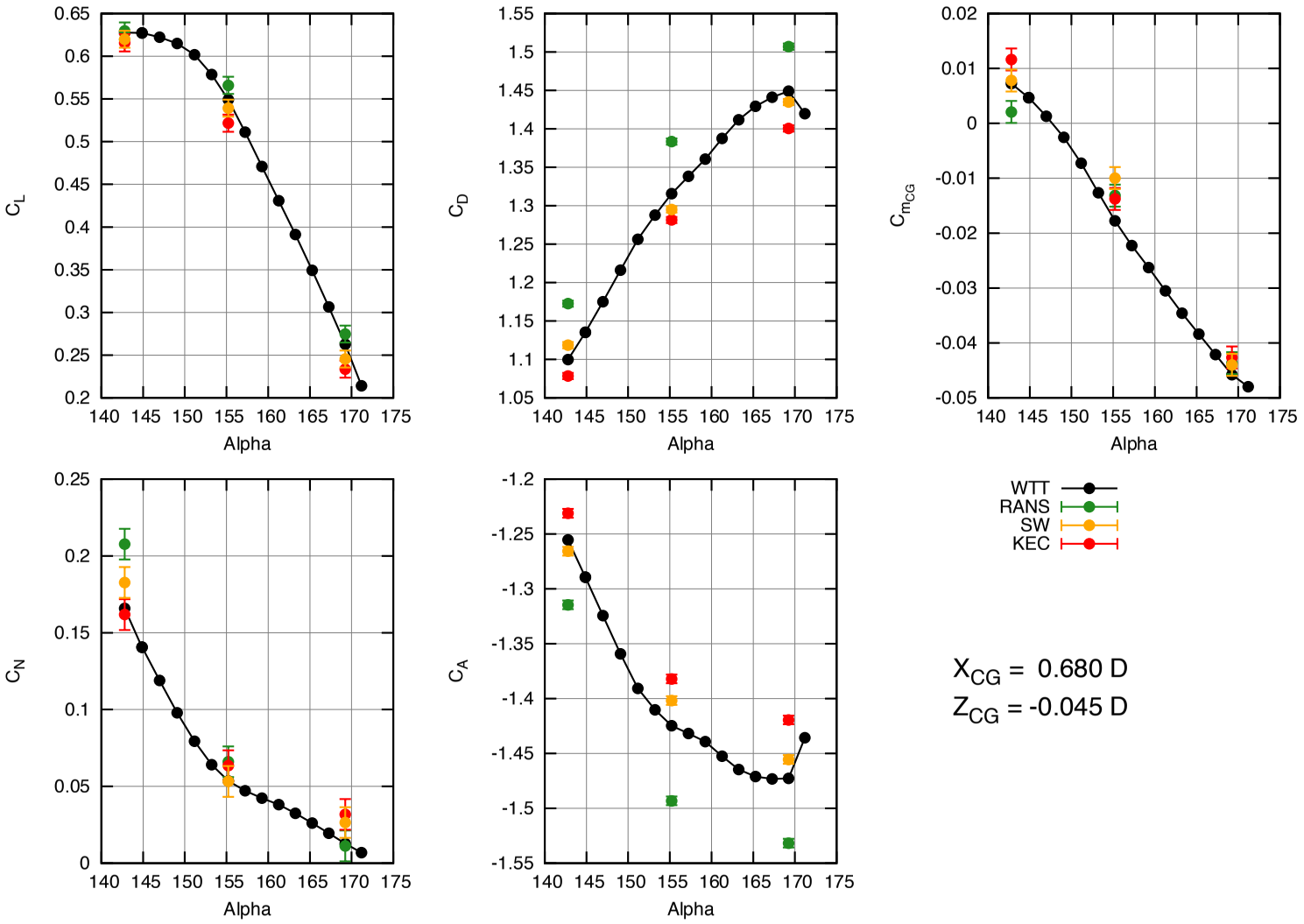

Figure 8. Comparison of aerodynamic loads for Mach 1.4.

Precent errors for each method at each angle of attack is listed in Table 3. Again, the RANS-KEC results stick out as being furthest from the tunnel data. Both DES methods perform well, with the Steiger-Warming results showing a distinct advantage over the range of cases and coefficients. DES-KEC, while not an improvement over SW for all cases, remains competitive in this regime and maintains an error magnitude less than 10% for most coefficients. It should be noted that where test results were near zero, the percent error values are somewhat deceiving.

	RANS-KEC			DES-SW			DES-KEC		
	140°	155°	170°	140°	155°	170°	140°	155°	170°
C_L	0.3	3.03	4.4	1.24	2.38	6.81	1.89	5.04	10.5
C_D	6.62	5.15	3.96	1.6	1.87	0.21	2.13	2.6	2.91
C_N	25.26	23.5	9.06	9.8	1.67	137.63	3.24	18.87	146.28
C_A	-4.71	-4.8	-3.97	-0.74	-1.95	-0.03	-2.06	-3.	-3.17
$C_{m_{CG}}$	71.32	-25.95	-4.66	9.68	-42.76	-3.08	64.13	-22.66	-6.51

Table 3. Table of percent error for Mach 1.4 results.

B. Mach 0.95

The next Mach number considered was transonic, Mach 0.95. As compared to the supersonic case, there is more significant unsteadiness and the presence of expansion causing areas of supersonic flow. This is a more dynamic case with an expanded wake region. For models with varied levels of unsteadiness (RANS versus DES) and different levels of dissipation (SW versus KEC), the computational results begin to show more significant spread.

Figure 9 shows a comparison of the aerodynamic coefficients for this Mach number. The RANS-KEC set of cases are clearly outperformed across the board. In general, the DES-KEC cases lie nearly on top of the wind tunnel data with the largest observable excursions seen in normal force (C_N) due to its relatively low magnitude as compared to the convergence tolerance. DES-SW does a fair job across the board but shows a more pronounced error at this tunnel condition.

Table 4 shows the precent error for all cases at this Mach number. Generally, the results are good for the DES methods. It is alarming to see the error in the thousands for C_N - this is due to admittedly poor performance but also to the very small magnitude in the measured coefficient from the tunnel. $C_{m_{CG}}$ also shows pronounced error due to the small magnitude.

	RANS-KEC			DES-SW			DES-KEC		
	140°	155°	170°	140°	155°	170°	140°	155°	170°
C_L	23.49	28.57	9.41	7.79	4.91	18.75	2.91	3.03	27.87
C_D	18.7	17.09	16.43	8.32	8.73	4.72	2.76	2.27	0.6
C_N	9.1	69.95	55870.83	11.5	37.54	186754.17	35.8	42.33	217016.67
C_A	-20.31	-19.03	-16.24	-8.14	-8.09	-4.08	-0.85	-1.37	-1.34
$C_{m_{CG}}$	24.72	118.93	-11.16	21.76	38.85	-2.9	4.02	77.79	-1.28

Table 4. Table of percent error for Mach 0.95 results.

One case, the $\alpha = 170°$, RANS-KEC appears to do a better job at matching C_L and C_N while missing to a great extent the other components. Similarly, the other two models appear to perform uncharacteristically poorly at this condition. Taking a look at the pressure port measurements can highlight what exactly might be causing this improved performance.

Figures 29 and 30 shows two different types of plots that are helpful in examining the pressure ports on the model. The first type of plot is a freckle plot (Fig. 29(a-c)). These freckle plots show a contour of pressure coefficient (C_P) on the surface as computed from the numerical results. The colored spheres represent the pressure ports from the test and they are colored by the experimental C_P as measured. Perfect agreement in surface pressure measurements would be characterized by colored spheres blending seamlessly into the contour on the capsule.

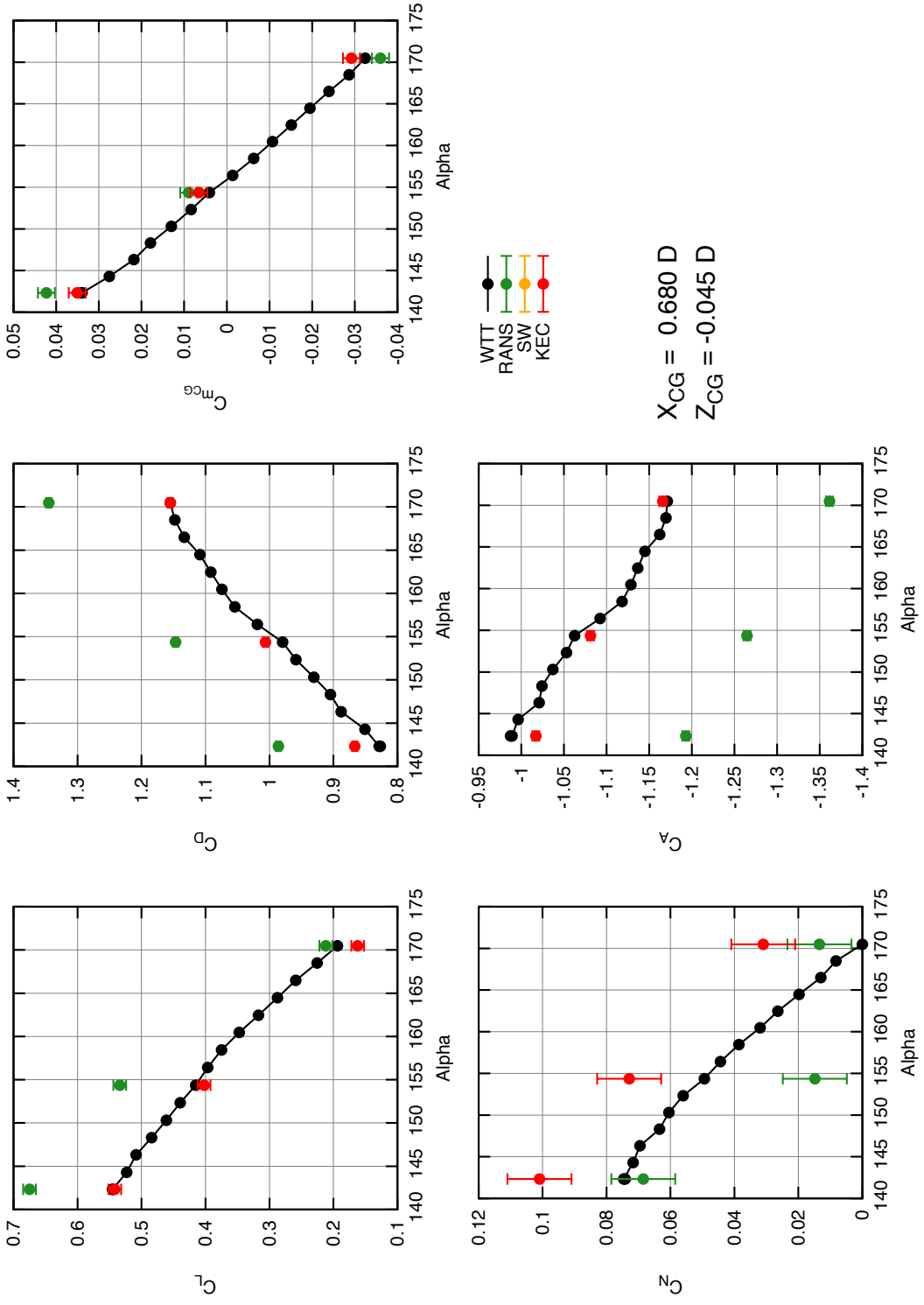

Figure 9. Comparison of aerodynamic loads for Mach 0.95.

The other type of plot, shown in Fig. 30(a), shows a much more quantitative assessment of the agreement between the data sets along a Y=0 slice through the geometry (the pitch plane). Along the y-axis is C_P, running from high to low. The x-axis is a running length along the model with the center of the plot being in the center of the heatshield (full scale x-location of 186"). Moving from the center to the left is moving in the leeward direction ($\phi = 0°$) and moving to the right is in the windward direction ($\phi = 180°$). Shown on the bottom are illustrations of the cut's position relative to the geometry and a representative wind vector (in blue). On the plot itself are circles representing the wind tunnel data and lines representing the pressures from the CFD solutions for each of the techniques considered.

Taking a look at the freckle plots, Fig. 29(a-c), the first thing that stands out is how different the RANS-KEC pressure look from the rest of the cases. This method predicts a much lower pressure on the backshell than seen in the test or measured in the wind tunnel. Moving from DES-SW to DES-KEC, the pressure again rises on the backshell to become a much better match for the wind tunnel results. Figure 30(a) shows this same trend but with much more detail. All of the numerical models match the wind tunnel data very well on the heat shield, but as flow expands at the shoulder and finally separates on the conical portion they three lines diverge. Looking at the backshell data alone, it is again clear that DES-KEC closely matches the tunnel data on that portion of the geometry. Where all three methods have a hard time hitting the data is on the shoulder - each of the three models separates at a slightly different location and therefore expands to a different suction peak and a different recovery on the conic.

Originally, the goal was to compare why the RANS-KEC case appeared to compare better in C_L and C_N than the other two cases at this condition. It is clear that it is not due to the strength of its comparison but instead to luck or chance. The other two cases provide a more faithful comparison, but discrepancies between the leeward and windward sides do not average out to provide the correct integrated load. This is an important observation and underscores the importance of point measurements in validation - integrated quantities can hide all manner of sins.

C. Mach 0.5

The lowest Mach number considered in the analysis and the wind tunnel test was Mach 0.5. It is obviously the most unsteady of the conditions considered here and provided the largest difficulty for the numerical techniques considered. Similar to the Mach 0.95 case, this increase in the turbulent content and the massively-separated nature of the flow is expected to highlight differences between the fidelity of the numerics.

Figure 10 shows the integrated loads for the three conditions at this Mach number. Unlike the previous cases, there does not appear to be one method that outperforms the other - they all appear to have challenges. While not too much should be read into them, some patterns exist. RANS-KEC matches closest in the 'normal' forces (C_L and C_N), DES-SW does the best for the 'axial' forces (C_D and C_A), and DES-KEC stands out for C_{m_CG}.

Table 5 shows the precent error for all cases at this Mach number. As mentioned in the previous paragraph, the results are mixed. As with the Mach 0.95 results, several cases have precent error in the thousands due to the small magnitude in the measured coefficient.

	RANS-KEC			DES-SW			DES-KEC		
	140°	155°	170°	140°	155°	170°	140°	155°	170°
C_L	1.03	5.65	1.81	14.11	29.05	25.57	23.26	25.92	34.88
C_D	15.09	18.99	18.57	5.68	4.39	15.03	11.38	12.13	13.96
C_N	-151.98	-95.28	-552.59	-198.35	-275.89	-1321.19	-343.24	-306.54	-1586.89
C_A	-8.78	-16.75	-18.28	-2.15	-1.68	-13.93	-2.5	-5.2	-12.58
$C_{m_{CG}}$	20.05	49.24	-46.85	26.87	48.93	-66.29	4.34	23.83	-45.97

Table 5. Table of percent error for Mach 0.50 results.

In order to inspect the performance at a more fundamental level, freckle plots and line plots of pressure tap data prove insightful. The figures in the appendix will be reference in order to avoid duplicating such a large number of images. Each of these three cases will be examined in detail, but there are some general comments to be made concerning the CFD results at this Mach number. Similar to the Mach 0.95 case examined previously, the RANS-KEC results predict significantly incorrect pressures on the backshell of

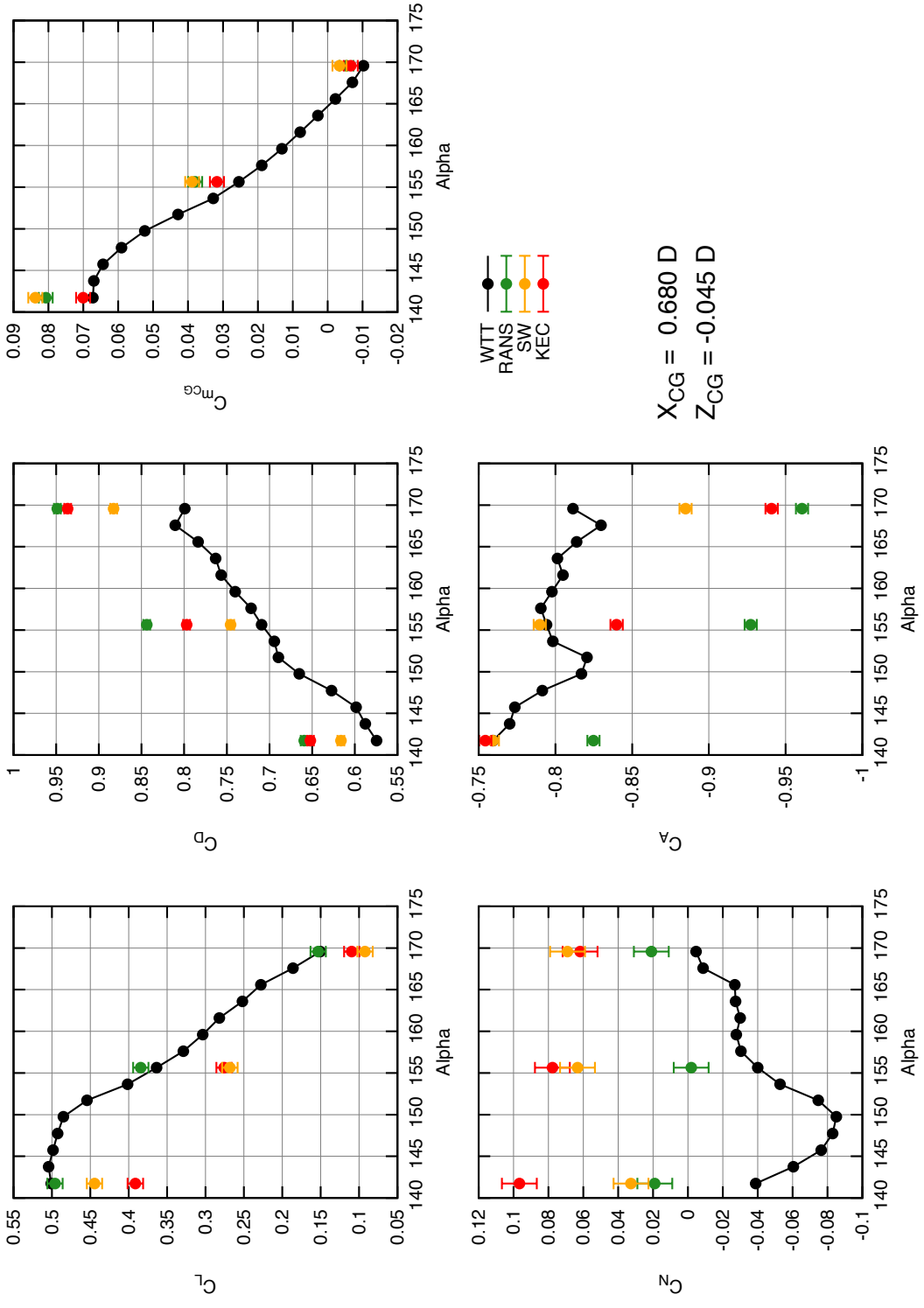

Figure 10. Comparison of aerodynamic loads for Mach 0.5.

the vehicle. The other cases also follow the previously examined trend with DES-SW providing a middling comparison and DES-KEC most frequently predicting the pressures correctly on the backshell. As is easily observed from Fig. 10, this does not translate into DES-KEC being the most accurate of the methods. This is because the prediction of separation on the shoulder - a case-specific phenomena - contributes greatly in the success of any one of these methods.

Starting with α =140°, Fig. **??**(a) shows that all three methods do a great job of matching the pressure in the $\phi = 0°$ cut. At the windward shoulder, though, the RANS-KEC is the only method that accurately predicts the suction peak, with DES-KEC being the worst. Moving to the $\phi = 90°$ cut, RANS-KEC falls behind the other methods and missed both the shoulder pressures and the backshell pressure. This time, DES-KEC is in highest agreement with the data. An interesting conclusion drawn from the $\phi = 180°$ views in the freckle plot Fig. **??**, is that DES-SW appears to predict the three-dimensionality of the separation on the shoulder with the other two methods either under- or over-predicting the width of the suction peak.. Even in this one case, the models show varying behavior and not one of them appears to be universally favored.

A similar assessment of Figs. 17 and 18 show a sightly different story. In these plots, RANS-KEC is furthest from the data in all respects but somehow still manages to be the most accurate predictor of normal force and lift. The suction peak again proves challenging for all of the methods, but DES-KEC proves the most faithful to the test data . DES-SW has similar difficulty as RANS-KEC, but not to the same extent, and both are arguably still attached for a portion of the backshell on the windward side. In both magnitude and trend, DES-KEC lies closest to the data for this condition.

The CFD results at $\alpha = 170°$ show similar performance between the cases as the $\alpha = 155°$ cases. DES-KEC seems to match the data for a created majority of the area on the capsule, but is challenged on the prediction of the suction peak and separation location. RANS-KEC and DES-SW have difficulty in the shoulder region as well, but also have more pronounced error on the backshell. It is fortunate for these latter two methods, though, that their error is comparable around the model (in the ϕ direction) and so it does not appear in the integrated quantities.

The results for this case imply that the dissipation provided by RANS and SW are sufficient to foul the overall pressure distribution, but not poor enough to completely pollute the integrated quantities, as evident by their fair performance in 10. Without the detail provided by the large distribution of pressure taps, it would not have been able to make this conclusion. While these dissipative models appear to perform well in the integrated loads, they are right for the wrong reasons.

V. Unsteady Results

In addition to the pressure taps mentioned earlier, the wind tunnel model was also instrumented with 12 unsteady pressure transducers. One of the transducers was placed internal to the model while the other 11 were installed on the surface of the backshell. Figure 11 shows a layout of the 11 taps on the backshell of the vehicle !!!!!4-5-6 wrong!!!!!. These unsteady results can help ensure that US3D is displaying the correct behavior in its representation of the unsteady flow. This data could further validate the conclusion discussed earlier that our temporal discretization was appropriate for the problem at hand.

In order to create a volume of data to ensure statistical convergence, the CFD cases required significant wall time. For this reason, computational results were only calculated for one condition in order to compare to experiment. The condition chosen was Mach 0.5, $\alpha = 140°$ due to its large degree of unsteadiness. It also showed a large disagreement between the methods which might indicate a variable unsteady response.

During the test, pressure measurements were made at a rate of 6400 Hz and recorded for a total of six seconds. After the test, these results were sampled using Welch's Method with a window of 0.2 seconds and a 50% overlap between windows. It was also passed through a low-pass anti-aliasing filter providing a bandwidth of 2500 Hz. The CFD data was down sampled to 6400 Hz and Welch's Method was empaled for 0.1 second windows with a a 50% overlap. A turkey window reduced aliasing error.

Figure 12 shows a comparison of the pressure signal at the backshell taps. Unfortunately, the CFD results are still quite noisy. This is due to the limited duration of the simulations - 0.4 seconds compared to the 6 seconds of wind tunnel data. Even so, it appears that the computations are, for may of the taps, picking up a frequency very close to the 130 Hz result reported from the tunnel. It isn't evident in all of the taps, but it is indicative of the dominate mode (that of the unsteady wake shedding) begin accurately resolved in the simulation.

Figure 11. Location of unsteady pressure transducers on the backshell of the model.

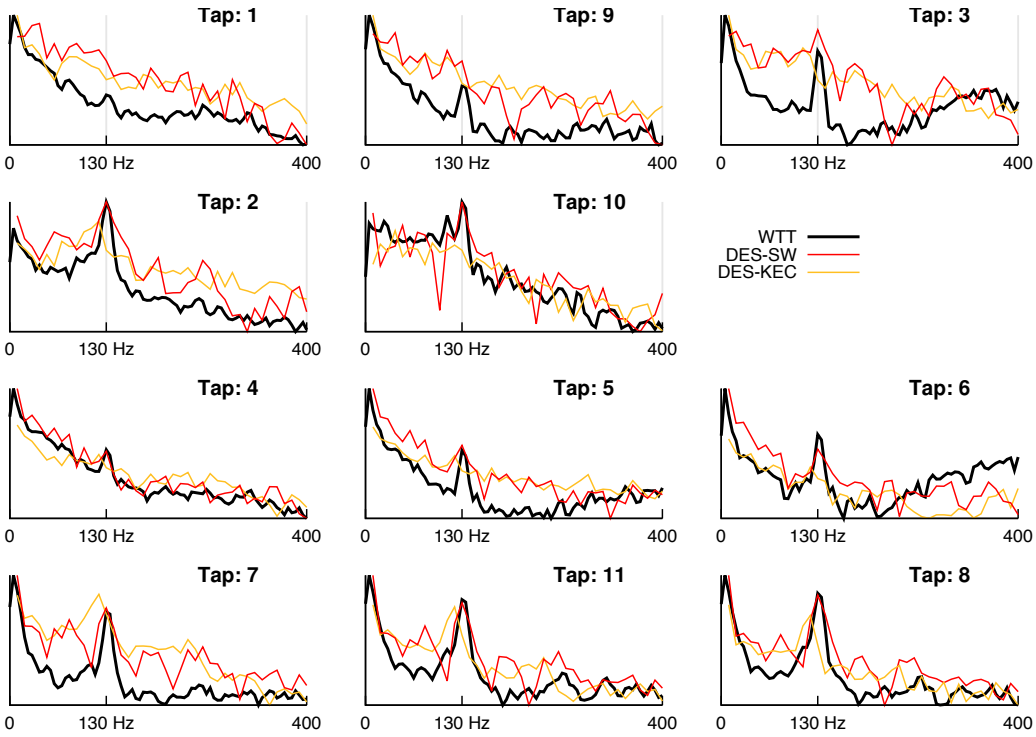

Figure 12. Energy spectra for pressure signal at the 11 backshell tap locations.

The unsteadiness of the wake drives the integrated loads, especially for this subsonic case. Looking at the unsteadiness in the integrated quantities, a similar comparison can be made between the wind tunnel and the CFD. C_m selected due to the strong signal it displays in this regard. Figure 13 shows the wind tunnel data for Tap 8 as a reference and the energy spectrum from the computationally calculated C_m. The signal is still noisy, but it confirms that the massively separated wake is displaying the correct shedding frequency.

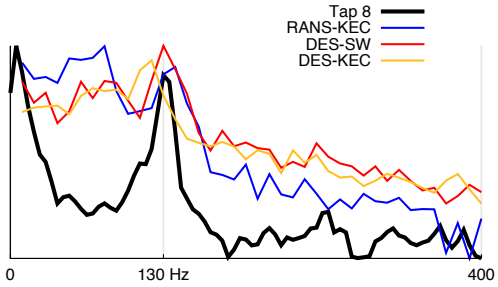

Figure 13. Energy spectrum for C_m in the CFD results. Tap 8 data included to identify wind tunnel peak frequency.

VI. Conclusions and Further Work

US3D's performance, using three available numerical approaches, was assessed at three angles of attack and three separate Mach numbers for for over a bluff body. The three Mach numbers were spread across three distinct flight regimes: supersonic, transonic, and subsonic. At all conditions, the predictions from the CFD code closely approximate the trend in the wind tunnel data and for the majority of the cases considered, the two DES schemes agreed with the data very well, supersonic and transonic cases in particular.

The RANS cases agreed with the test data in trend and correctly predicted the aerodynamic coefficients in several cases. These predictions were quire superficial, though, and upon further investigation of the pressures on the vehicle it is clear that the RANS model did not predict even the gross flow features correctly. Its success seems more to chance than ability.

All of the methods, for the one case considered here, resolve the bulk unsteadiness in the flowfield as characterized as the wake shedding frequency. This implies that the temporal discretization utilized here was not too aggressive and validates its selection. There was a slight spread between the methods, and future work will incorporate using the 4^{th}- and 6^{th}-order KEC fluxes due to their proven ability to better resolve unsteady phenomena.[7]

The hope of this work was to fully validate the DES-KEC numerical combination as sufficient to predict the aerodynamic performance of the MPCV CM and bluff body wakes in general. That desire was not completely realized, but of the models considered, it most accurately predicted the surface pressures over the largest portion of the vehicle and is arguably superior to the others. There remains work to do on improving the prediction of separation and there are several avenues considered here as further work.

An obvious means of improving the prediction of separation would be in modifying the turbulence model to better suit this problem. The Spalart-Allmaras model is a very capable model, but it remains a possibility that modifications to it or another model altogether could help in this regard. Additionally, further research into transition and perhaps using a transitional model might help more accurately simulate the wind tunnel test results. In nearly ever case, the wind tunnel separated in advance of the CFD. This hints at flow that was not fully turbulent and while trip dots were used in the tunnel, it is likely that the flow approaching the shoulder was not precisely as it was modeled.

One final avenue for improvement is in terms of grid quality. GridPro is a very capable tool and enabled the grids used in this analysis to be generated in a relatively rapid way. For complex geometries like this one, though, there remains a need to more accurately constrain the grid points to be properly aligned with critical geometric features. Examples include: perfect radial symmetry on the CM, grid lines aligned with the entirety of the round on the shoulder, backshell, and sting, and smooth stretching with a global stretching ratio limiter. Finally, an improved technique for corralling points without the excessive use of 'grid baffles' would ensure smooth transitions between regions of the flow. At the time of this writing, a code with that flexibility and was of use does not exist for block-zonal grids. As mentioned previously, it is not expected

that these improvements to grid quality will greatly impact the efficacy of the code, but they could provide enough of an improvement to close the gap between the predictions and the test.

Acknowledgements

This work was sponsored by the NASA Johnson Space Center Academic Fellowship. The views and conclusions contained herein are those of the authors and should not be interpreted as necessarily representing the official policies or endorsements, either expressed or implied, of NASA, Johnson Space Center, or the U.S. Government.

References

[1]Bell, J.H. "Test 5-CA Final Report, EG-CEV-06-19, NASA Johnson Space Center, March 2006

[2]Nompelis, I., Drayna, T. W., Candler, G. V., "Development of a Hybrid Unstructued Implicit Solver for the Simulation of Reacting Flows Over Complex Geometries," AIAA Paper 2004-2227, 2004

[3]Nompelis, I., Drayna, T. W., Candler, G. V., "A Parallel Unstructured Implicit Solver for Hypersonic Reacting Flow Simulation," AIAA Paper 2005-4867, June 2005

[4]Subbareddy, Pramod K. and Candler, Graham V., "A fully discrete, kinetic energy consistent finte-volume scheme for compressible flows," *Journal of Computational Physics* Vol. 228, 2009, pp. 1347-1364

[5]Ducros, F., Ferrand, V., Nicoud, F., Weber, C., Darracq, D., Gacherieu, C., and Poinsot, T., "Large-Eddy Simulation of the Shock/Turbulence Interaction," *Journal of Computational Physics* Vol. 152, 1999, pp. 517549

[6]Olsen, Michael E., "Sting Interference Analysis for CA-05 Test: CEM CM in AUPT," CAP TN/CAP-45-01, NASA Ames Research Center, April 2007

[7]Bartkowicz, M., "Numerical Simulations of Hypersonic Boundary Layer Transition," Dissertation, The University of Minnesota, 2012

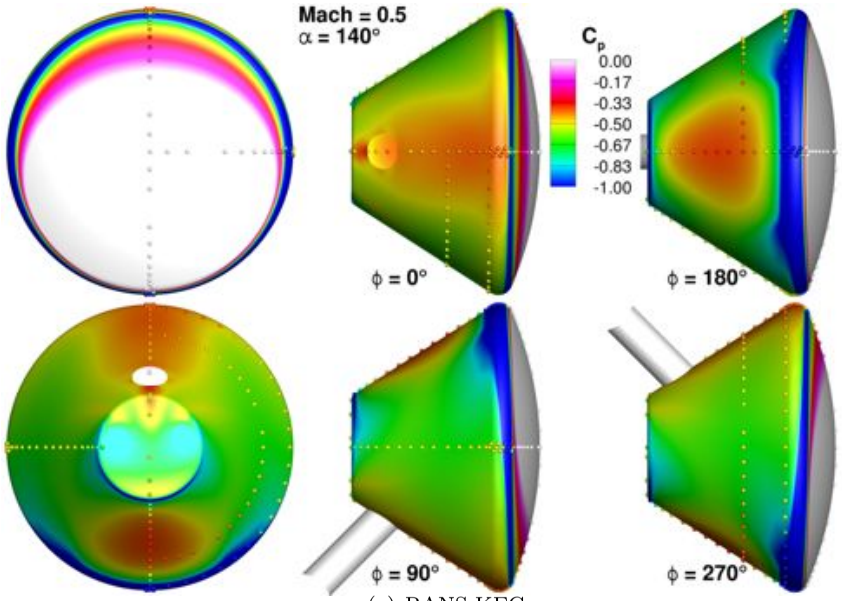

(a) RANS-KEC

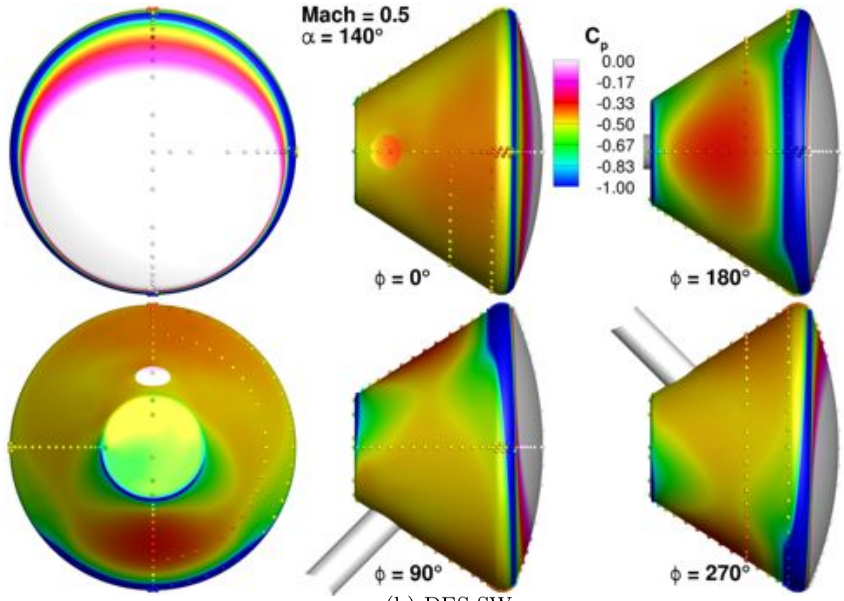

(b) DES-SW

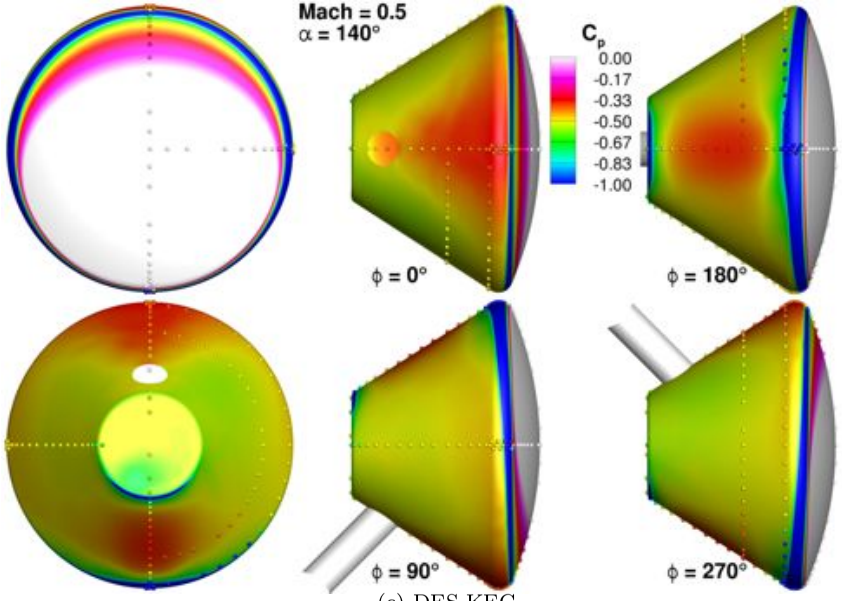

(c) DES-KEC

Figure 14. Freckle plots of pressure tap data for Mach 0.50, $\alpha = 140^\circ$ cases.

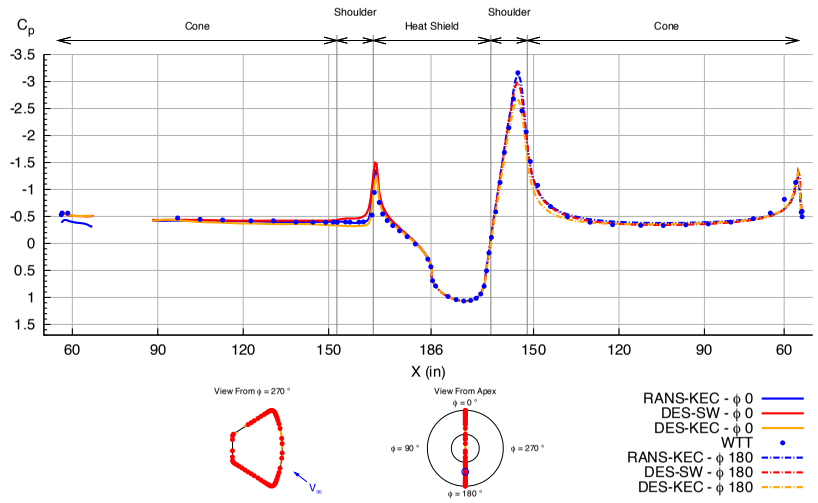

(a) $\phi = 0°$

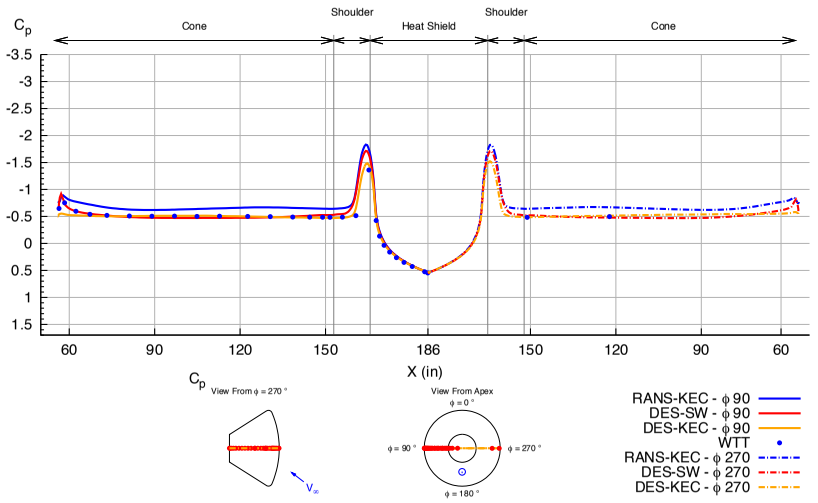

(b) $\phi = 90°$

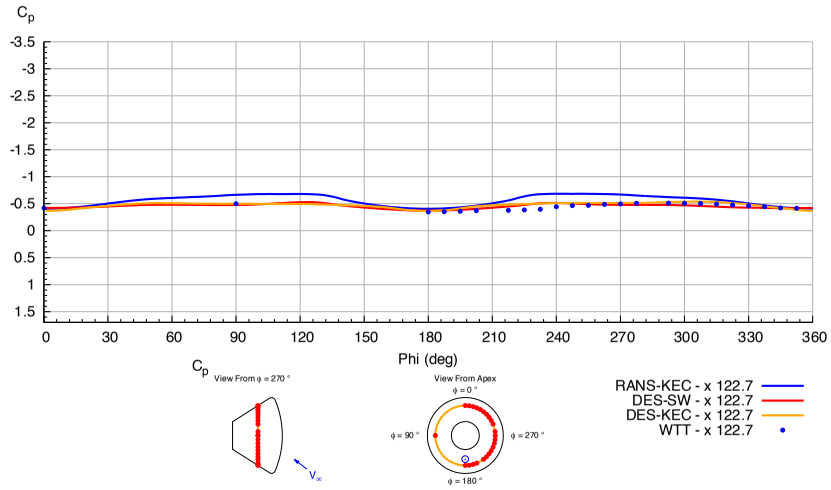

(c) X = 122.7”

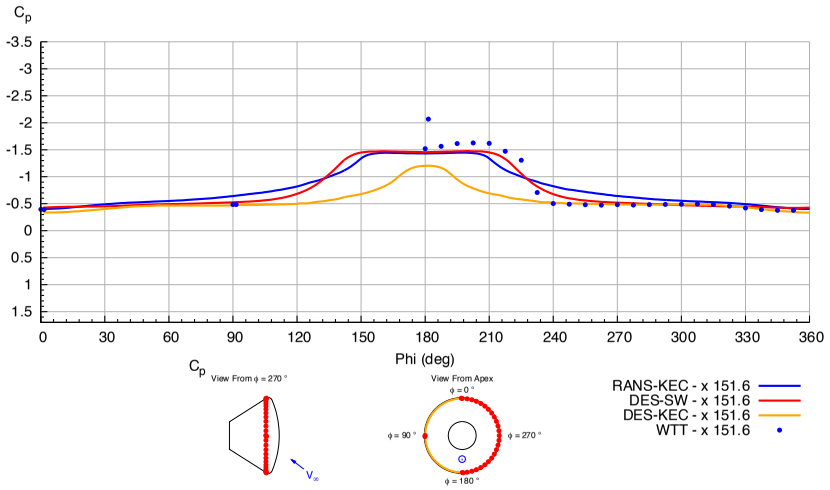

(d) X = 151.6”

Figure 15. Line plots of pressure tap data for Mach 0.50, $\alpha = 140°$ cases at various cuts along the fullscale geometry.

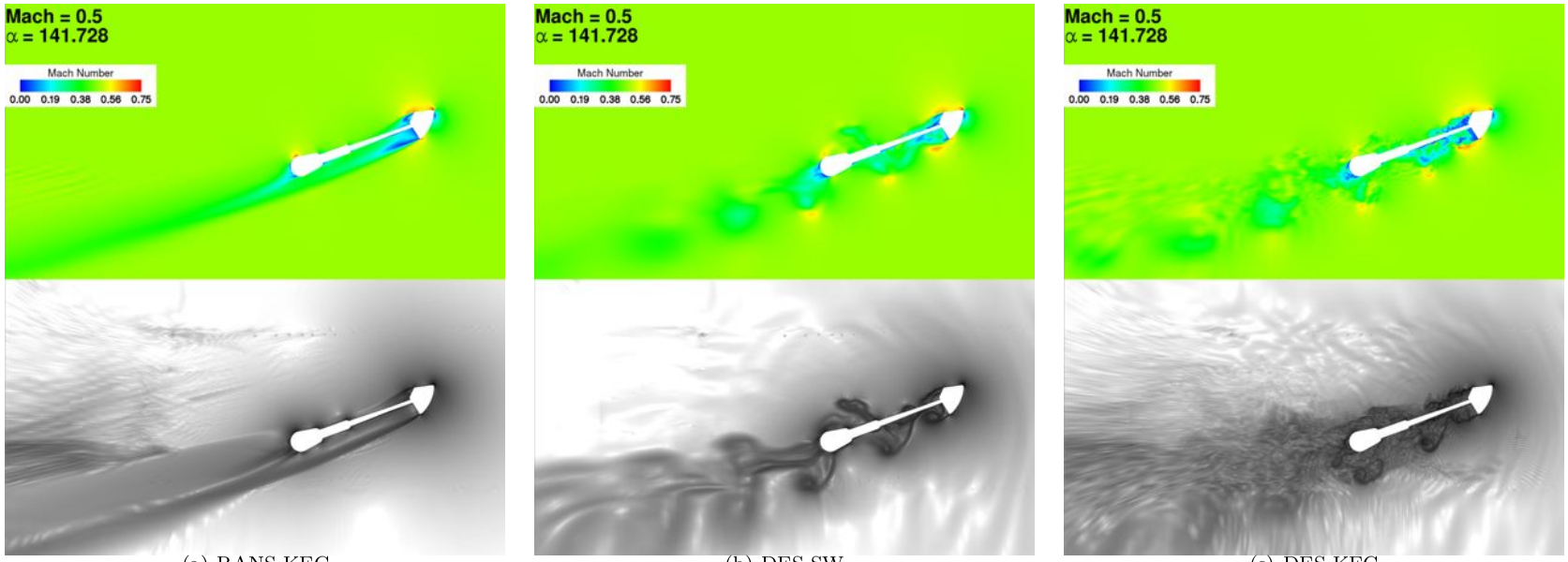

(a) RANS-KEC (b) DES-SW (c) DES-KEC

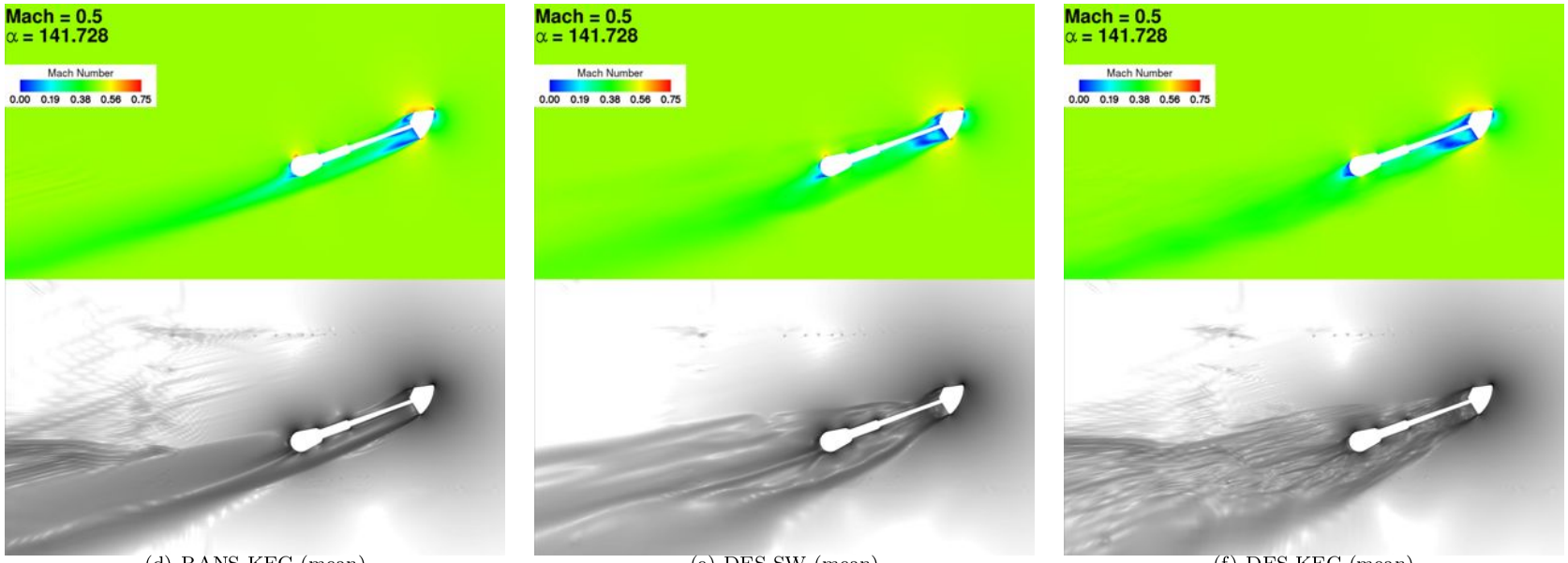

(d) RANS-KEC (mean) (e) DES-SW (mean) (f) DES-KEC (mean)

Figure 16. Plots of Mach number and log of density-gradient magnitude for both instantaneous and averaged cuts through the pitch plane (Y=0) at Mach 0.50, $\alpha = 140^\circ$.

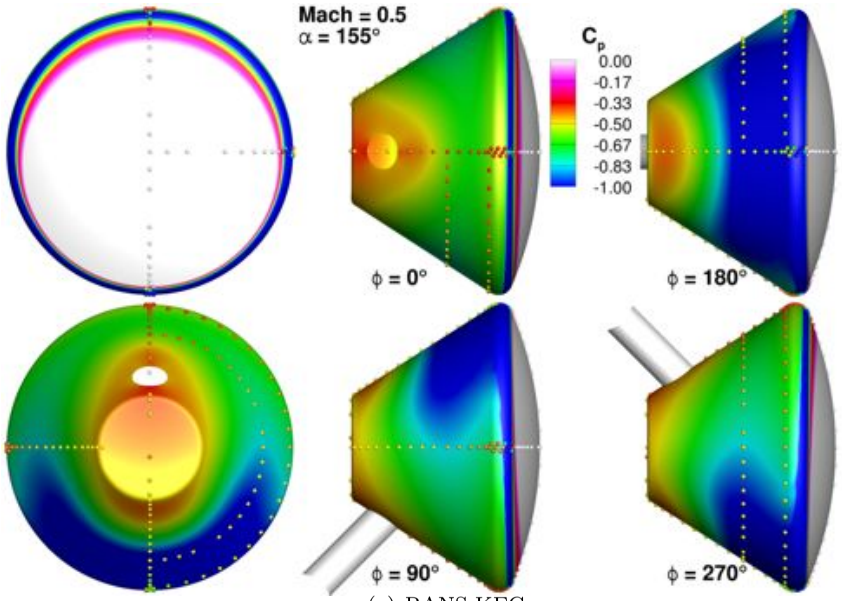

(a) RANS-KEC

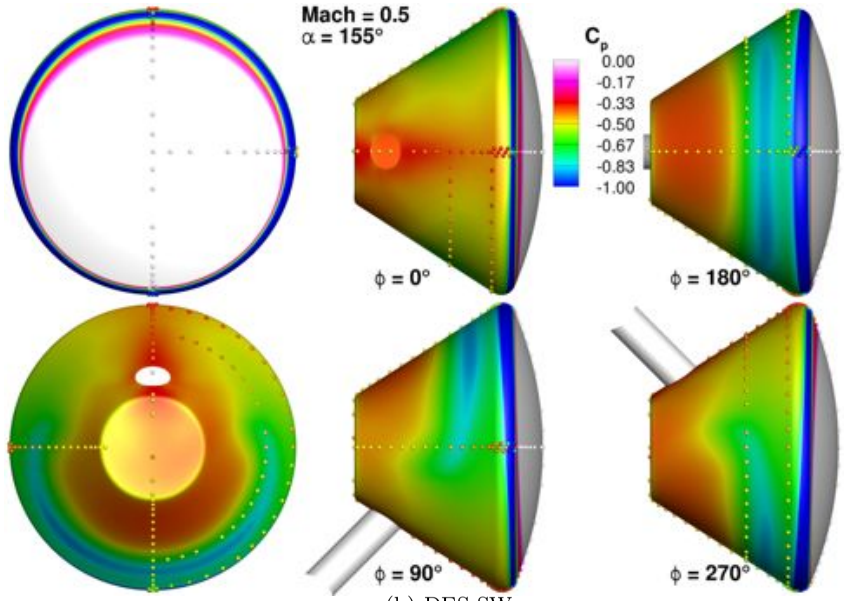

(b) DES-SW

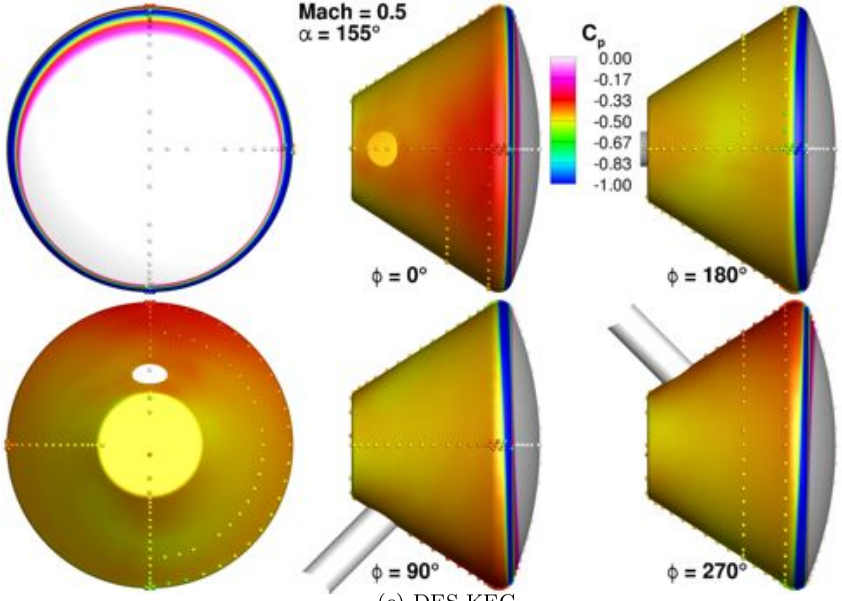

(c) DES-KEC

Figure 17. Freckle plots of pressure tap data for Mach 0.50, $\alpha = 155°$ cases.

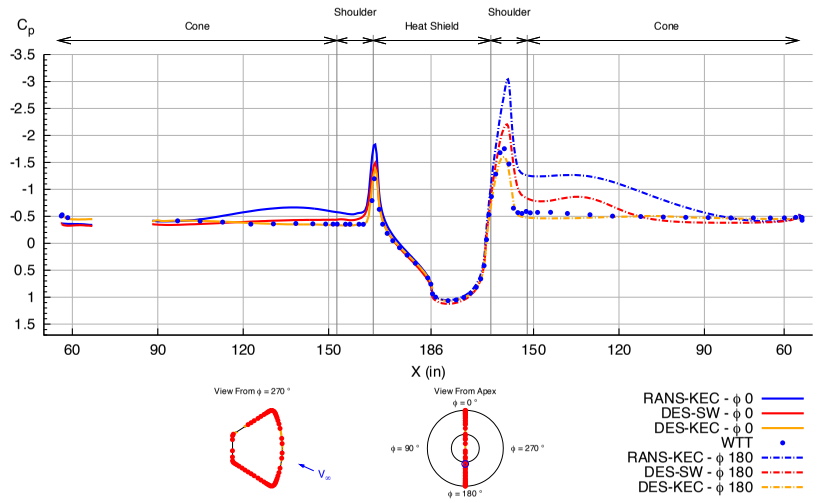

(a) $\phi = 0°$

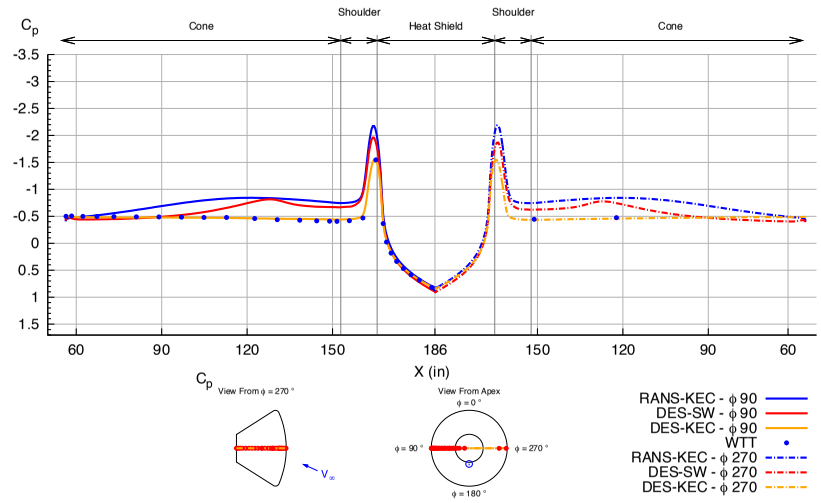

(b) $\phi = 90°$

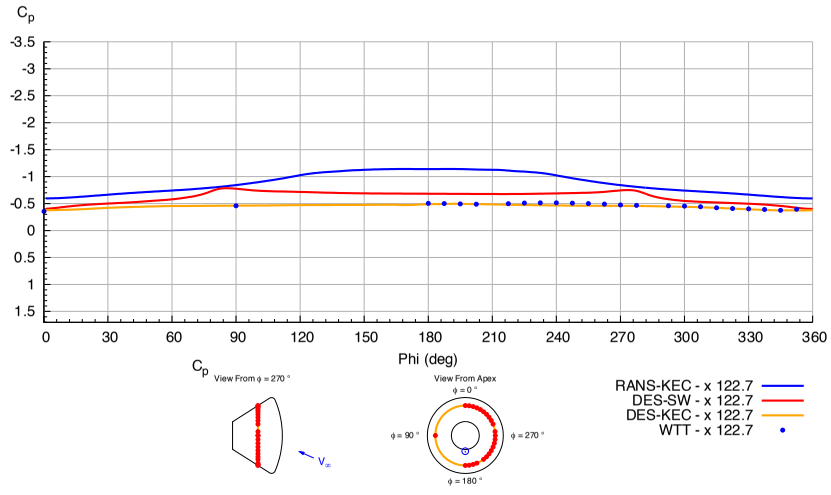

(c) X = 122.7”

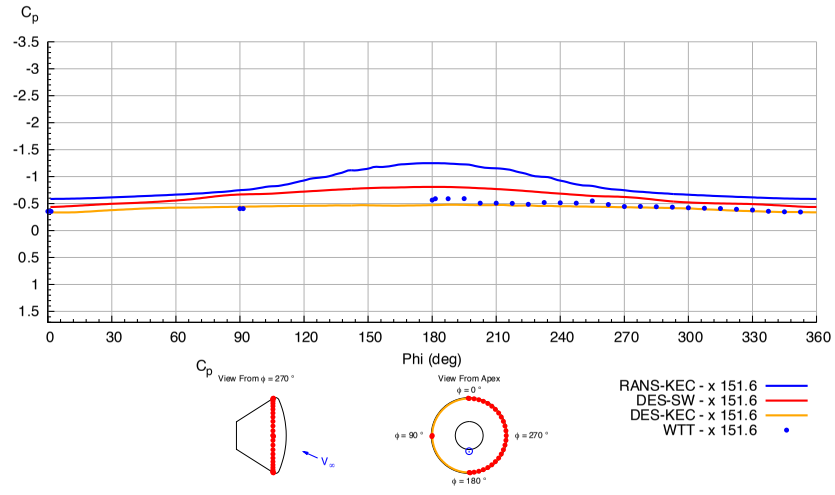

(d) X = 151.6”

Figure 18. Line plots of pressure tap data for Mach 0.50, $\alpha = 155°$ cases at various cuts along the fullscale geometry.

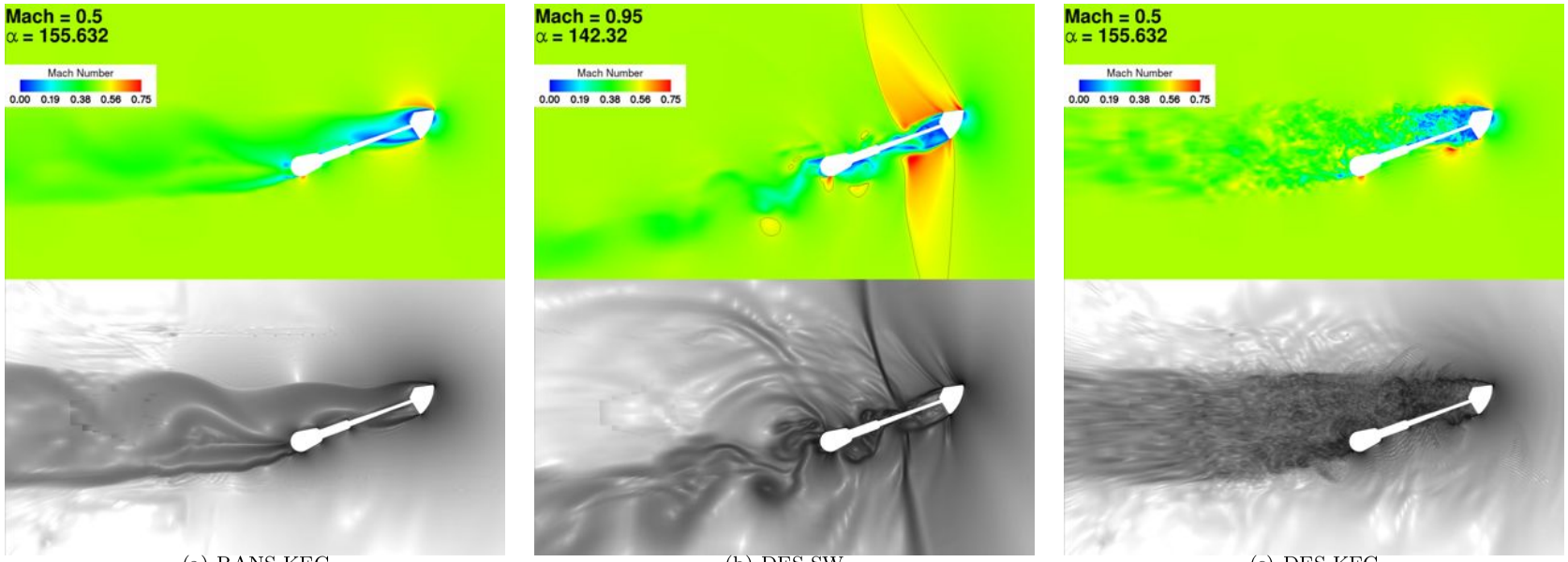

(a) RANS-KEC (b) DES-SW (c) DES-KEC

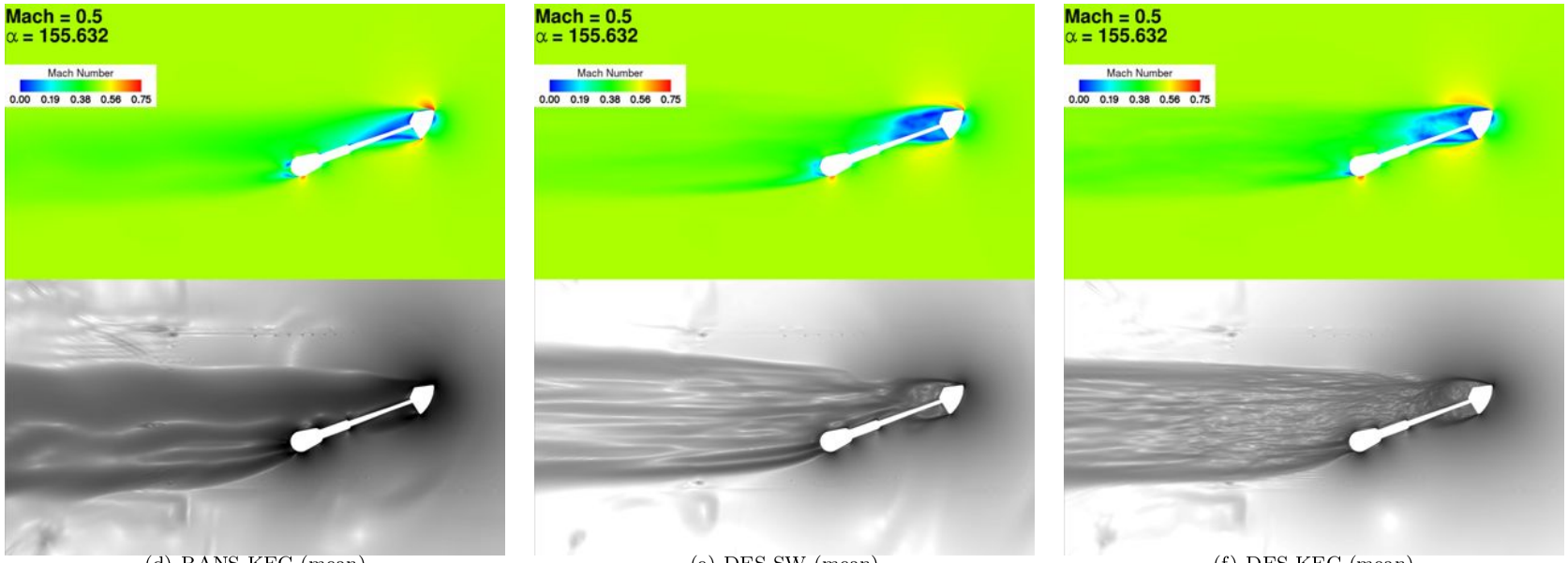

(d) RANS-KEC (mean) (e) DES-SW (mean) (f) DES-KEC (mean)

Figure 19. Plots of Mach number and log of density-gradient magnitude for both instantaneous and averaged cuts through the pitch plane (Y=0) at Mach 0.50, $\alpha = 155^\circ$.

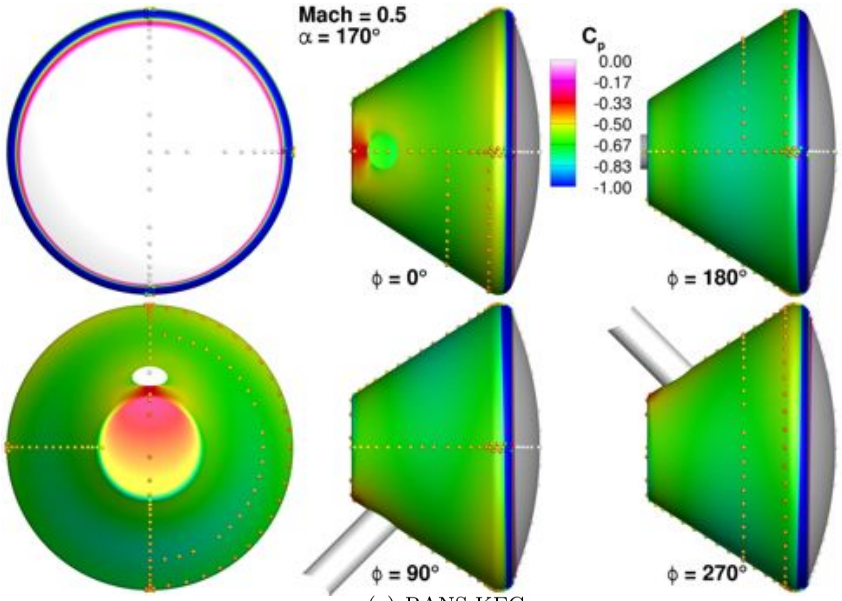

(a) RANS-KEC

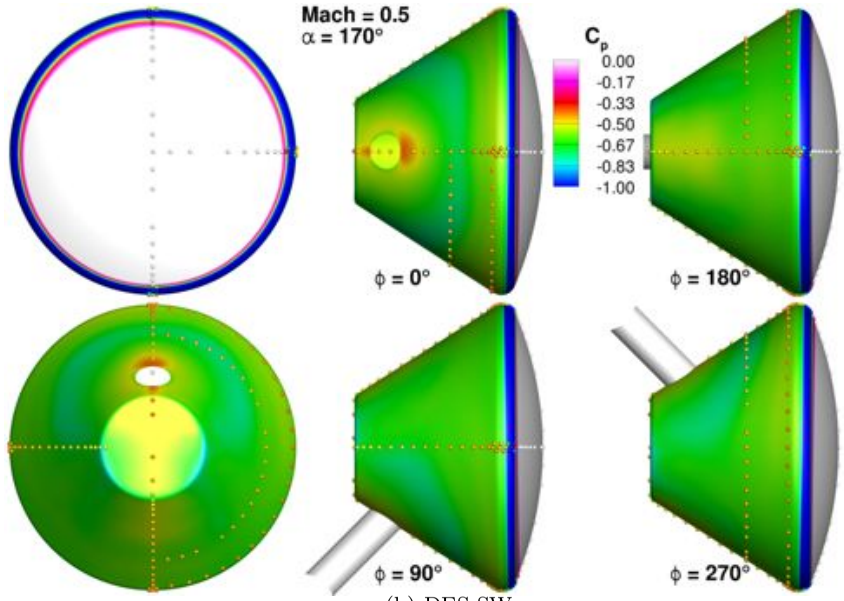

(b) DES-SW

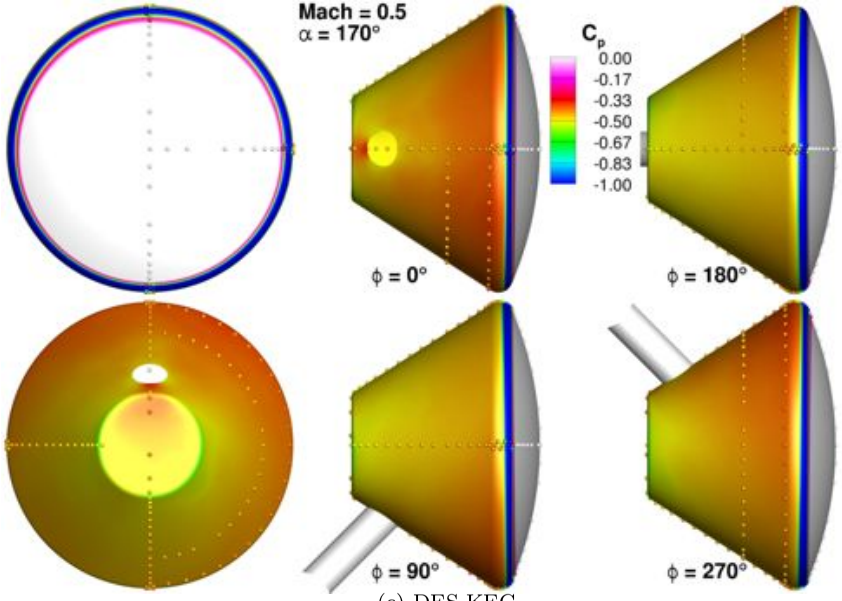

(c) DES-KEC

Figure 20. Freckle plots of pressure tap data for Mach 0.50, $\alpha = 170°$ cases.

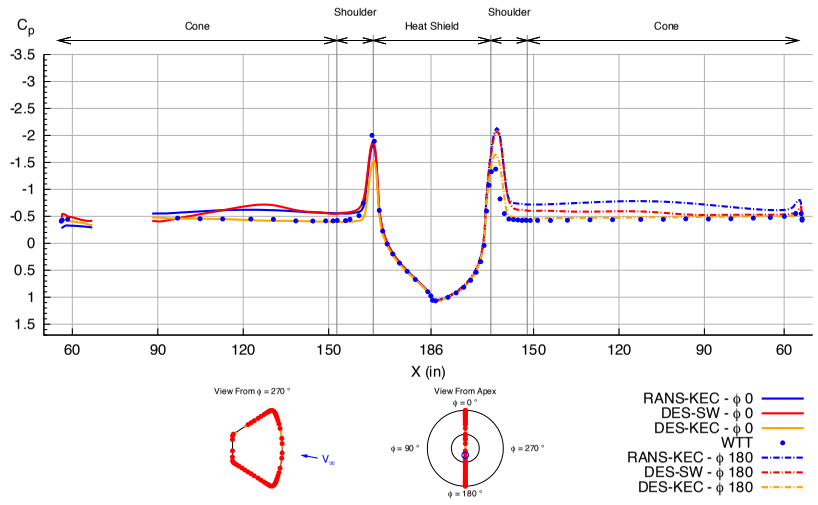

(a) $\phi = 0°$

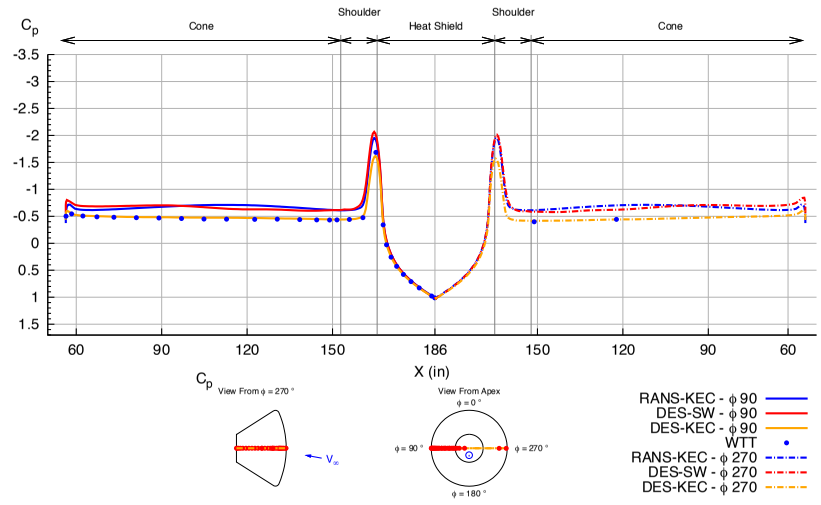

(b) $\phi = 90°$

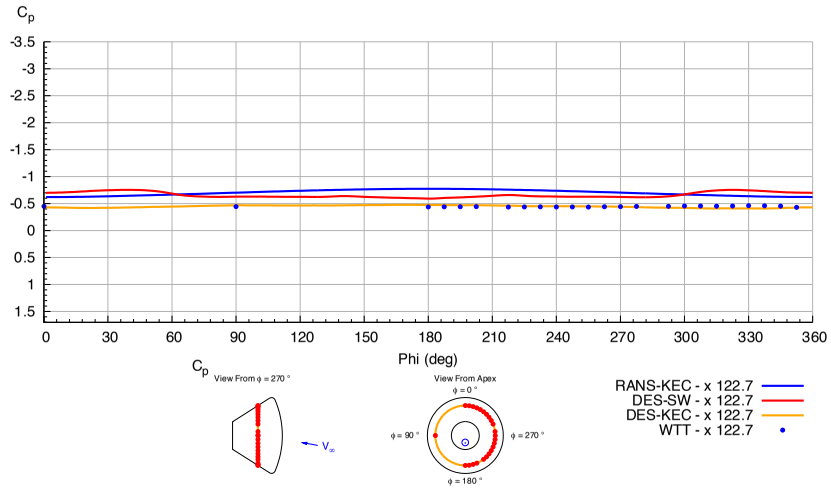

(c) X = 122.7”

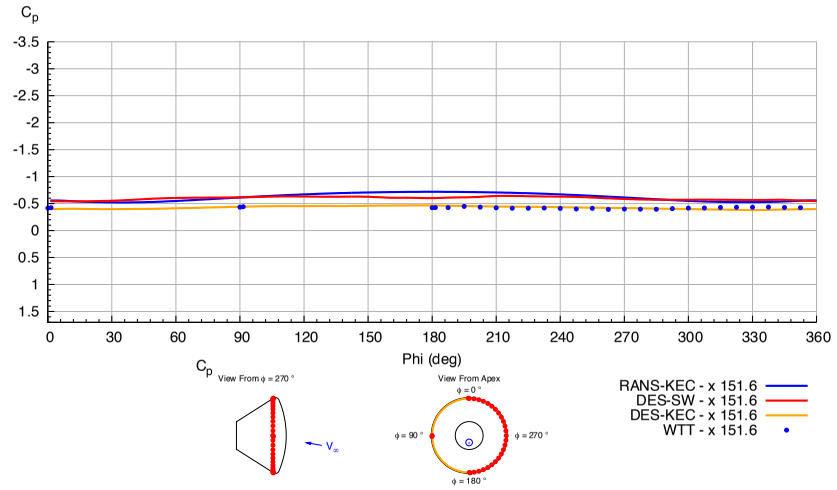

(d) X = 151.6”

Figure 21. Line plots of pressure tap data for Mach 0.50, $\alpha = 170°$ cases at various cuts along the fullscale geometry.

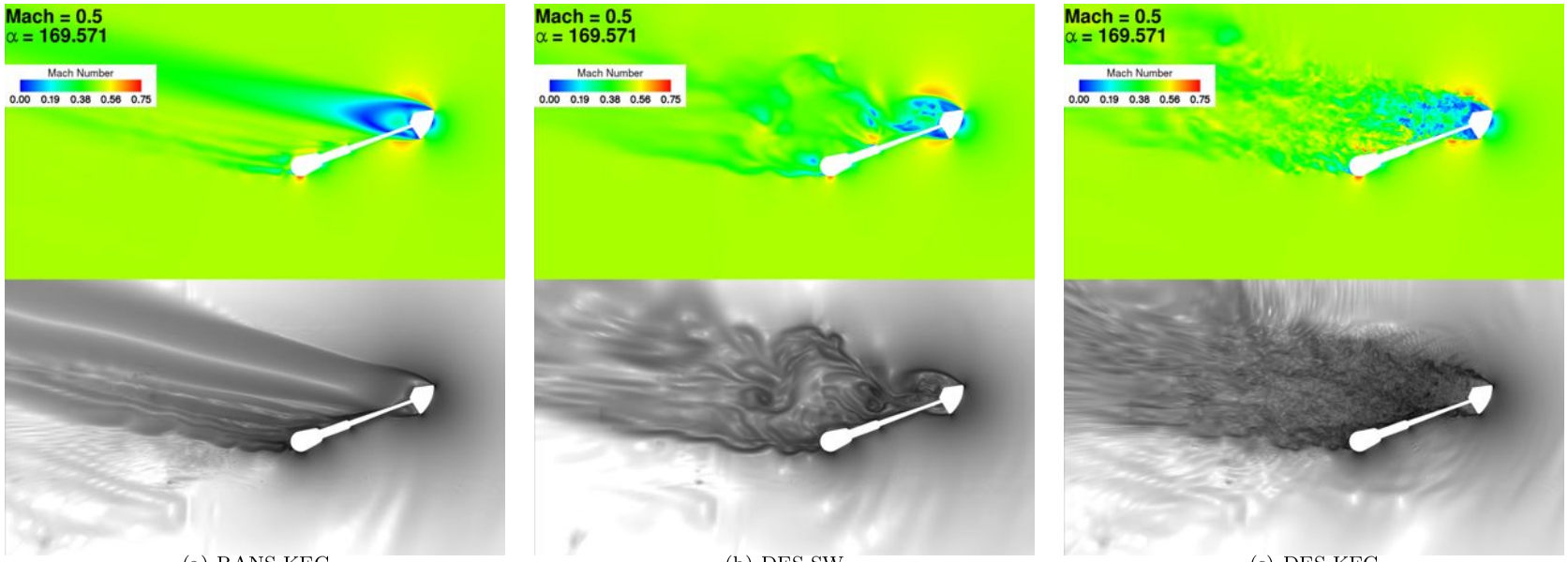

(a) RANS-KEC (b) DES-SW (c) DES-KEC

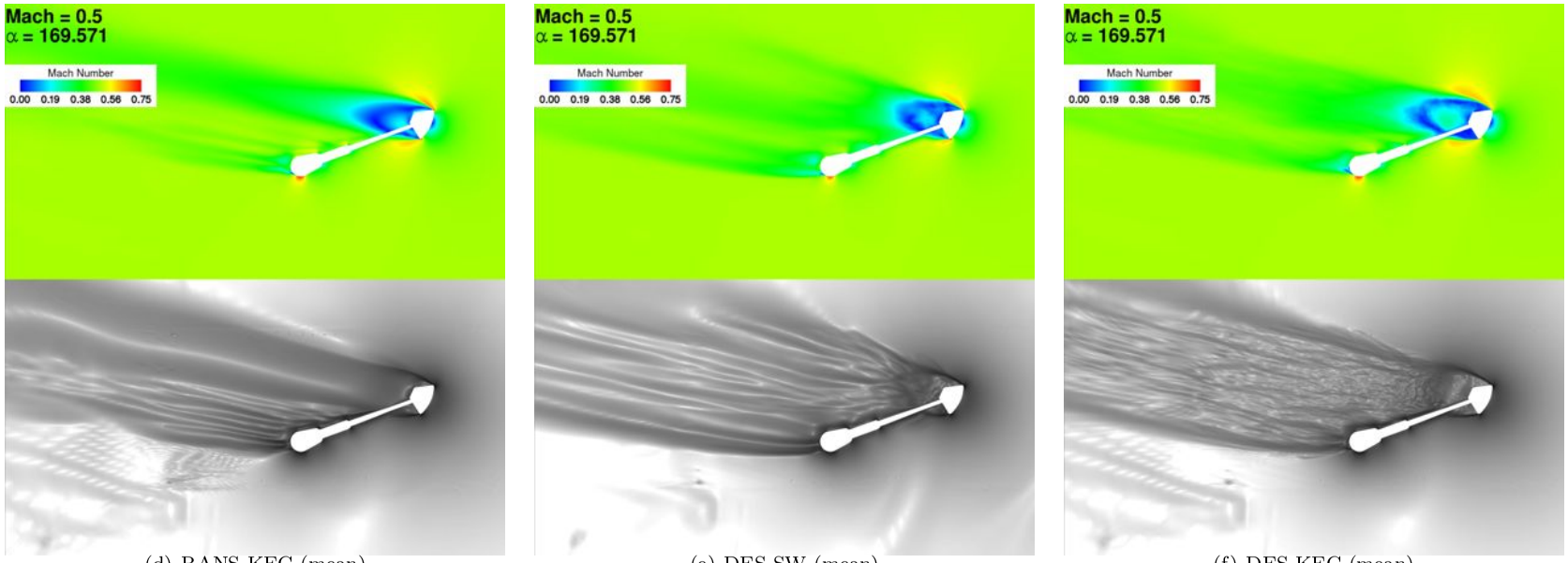

(d) RANS-KEC (mean) (e) DES-SW (mean) (f) DES-KEC (mean)

Figure 22. Plots of Mach number and log of density-gradient magnitude for both instantaneous and averaged cuts through the pitch plane (Y=0) at Mach 0.50, $\alpha = 170^\circ$.

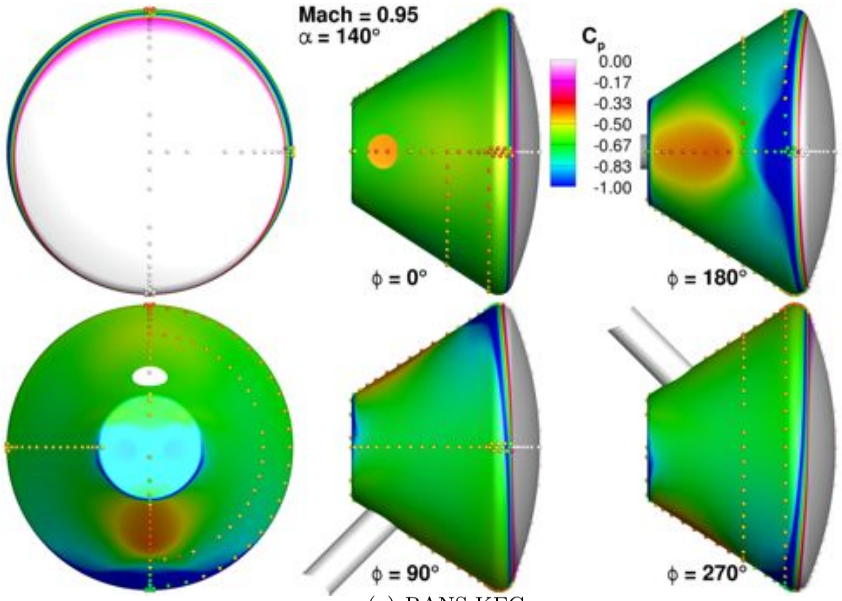

(a) RANS-KEC

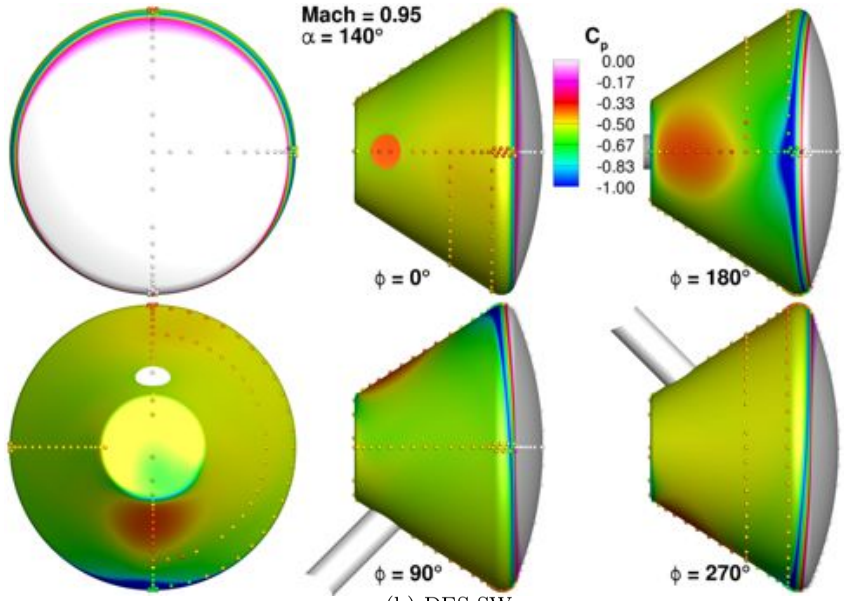

(b) DES-SW

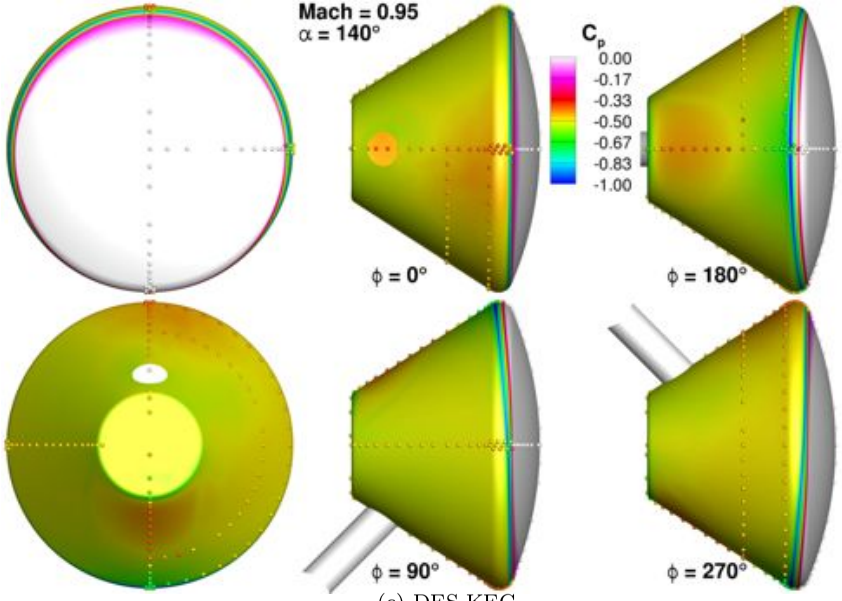

(c) DES-KEC

Figure 23. Freckle plots of pressure tap data for Mach 0.95, $\alpha = 140^\circ$ cases.

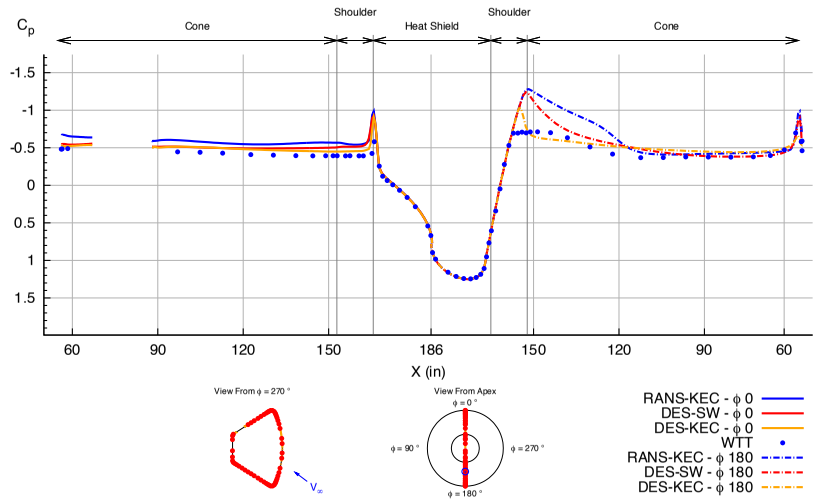

(a) $\phi = 0°$

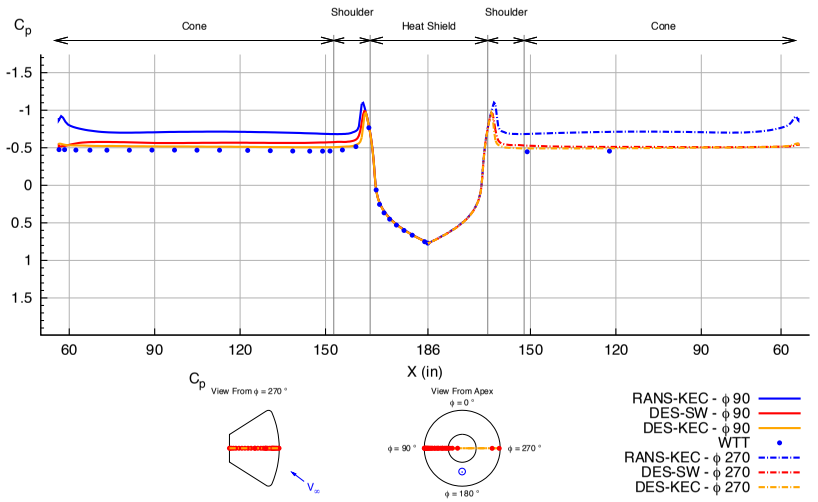

(b) $\phi = 90°$

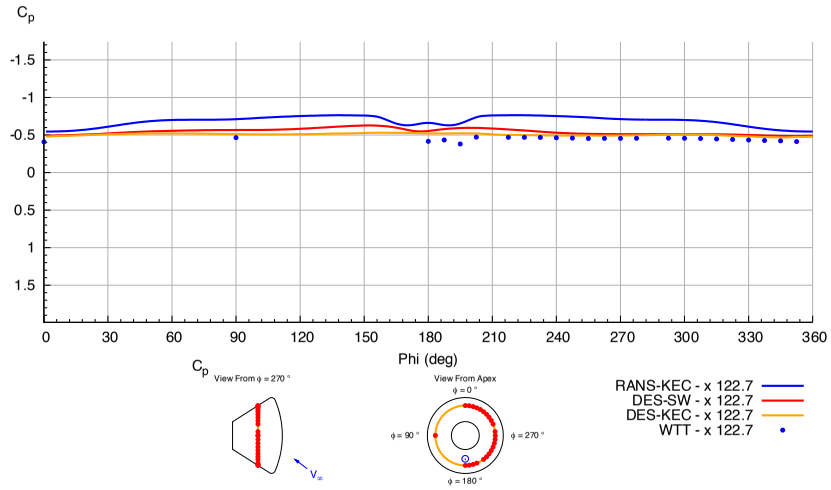

(c) X = 122.7”

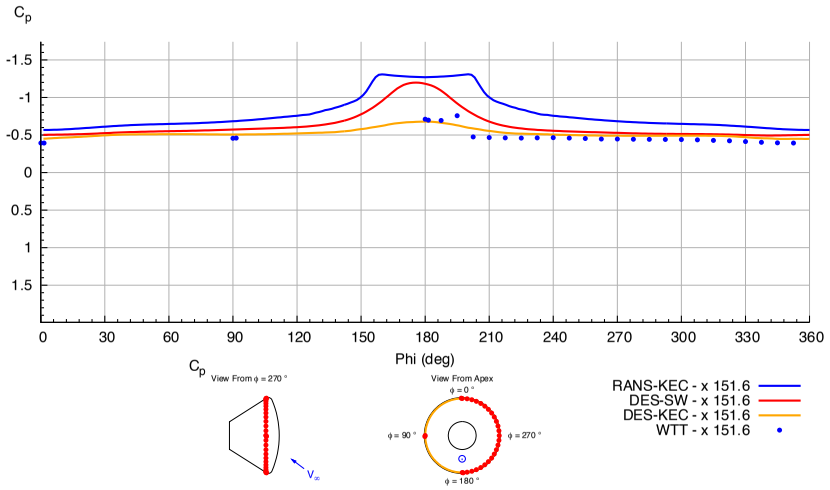

(d) X = 151.6”

Figure 24. Line plots of pressure tap data for Mach 0.95, $\alpha = 140°$ cases at various cuts along the fullscale geometry.

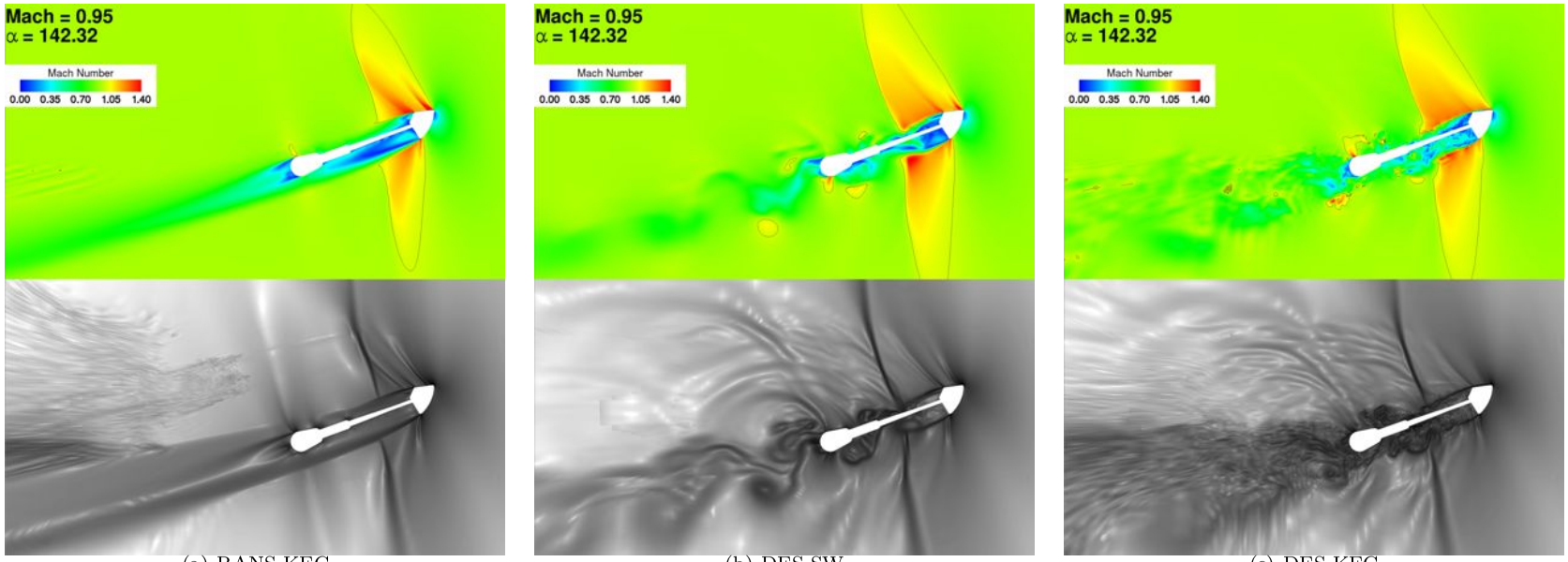

(a) RANS-KEC (b) DES-SW (c) DES-KEC

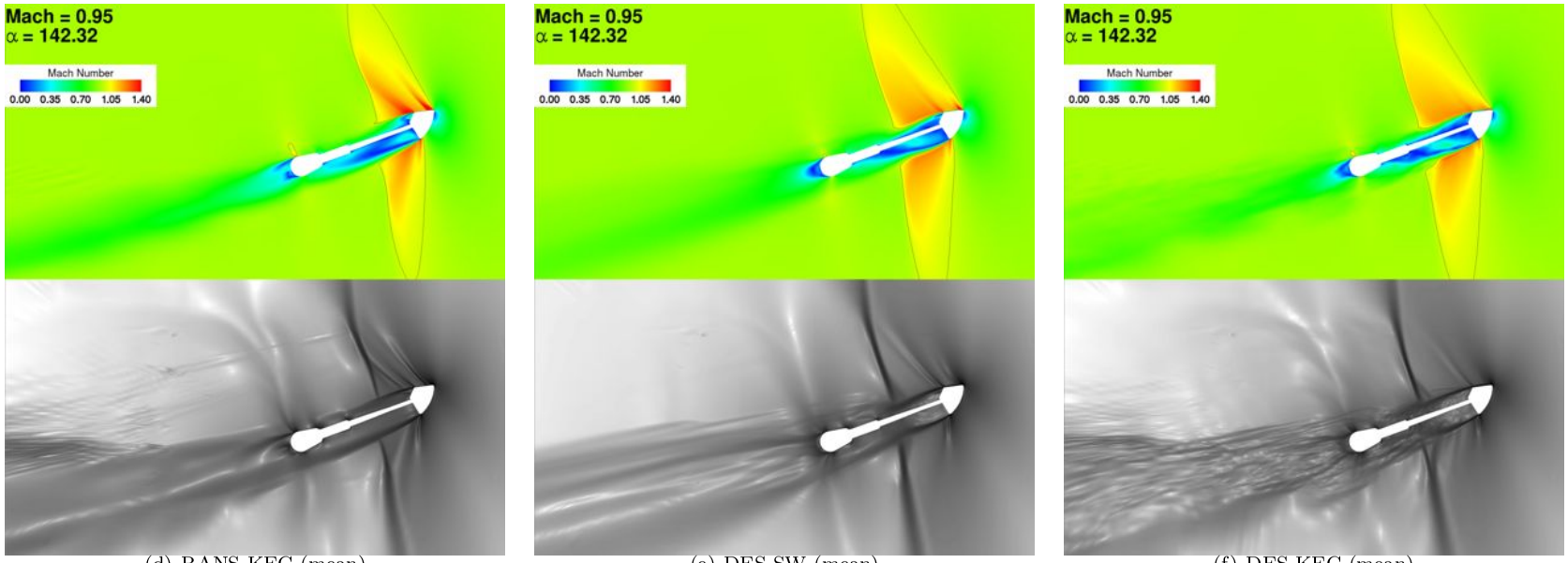

(d) RANS-KEC (mean) (e) DES-SW (mean) (f) DES-KEC (mean)

Figure 25. Plots of Mach number and log of density-gradient magnitude for both instantaneous and averaged cuts through the pitch plane (Y=0) at Mach 0.95, $\alpha = 140^\circ$.

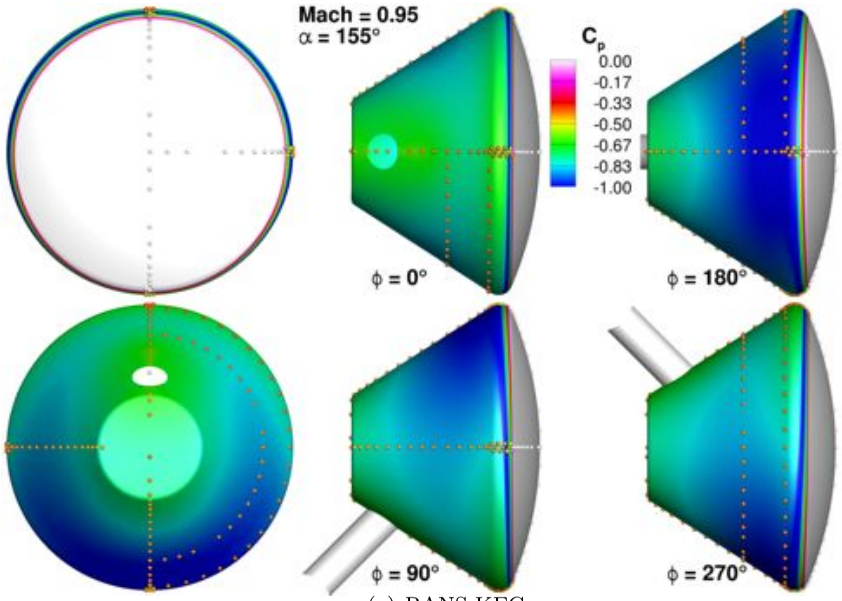

(a) RANS-KEC

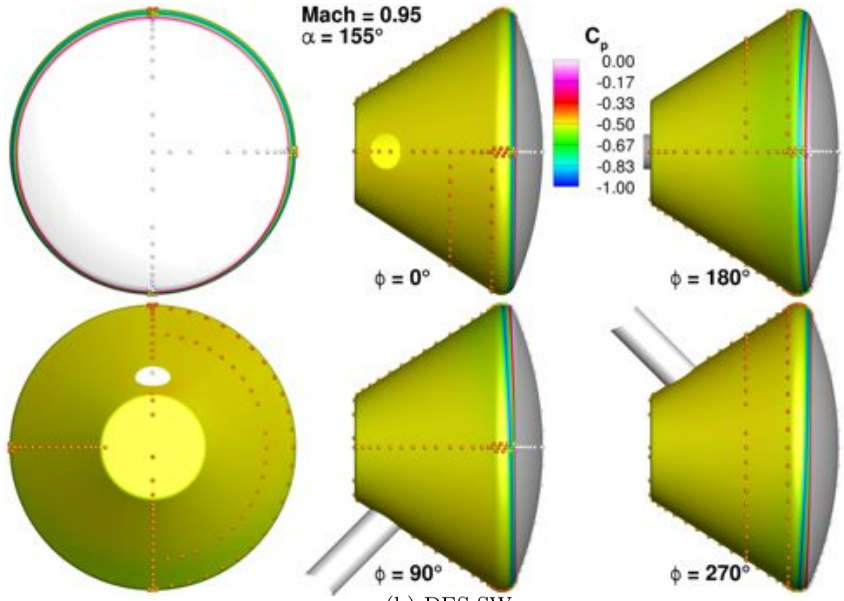

(b) DES-SW

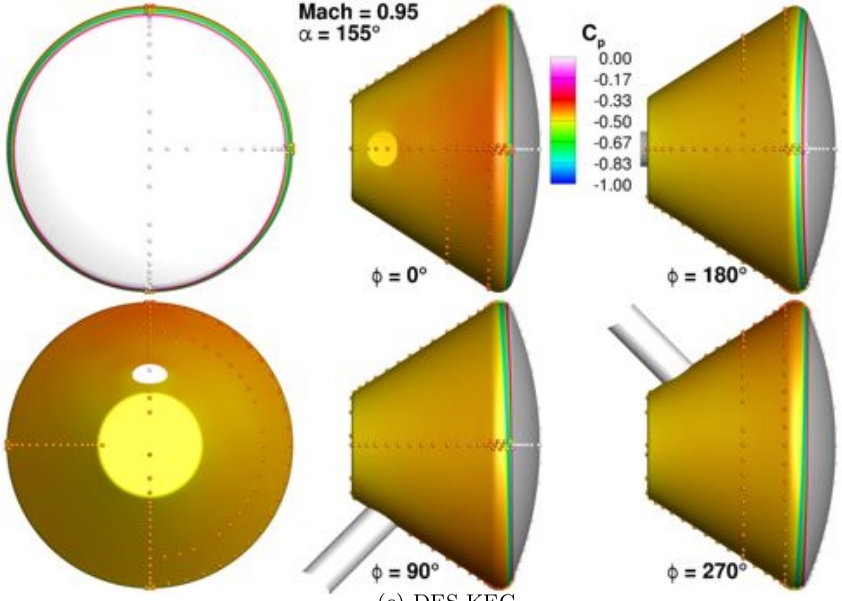

(c) DES-KEC

Figure 26. Freckle plots of pressure tap data for Mach 0.95, $\alpha = 155°$ cases.

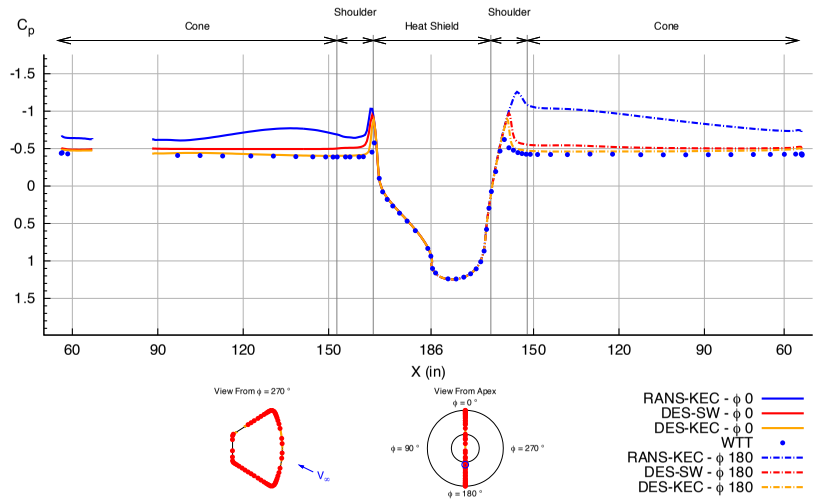

(a) $\phi = 0°$

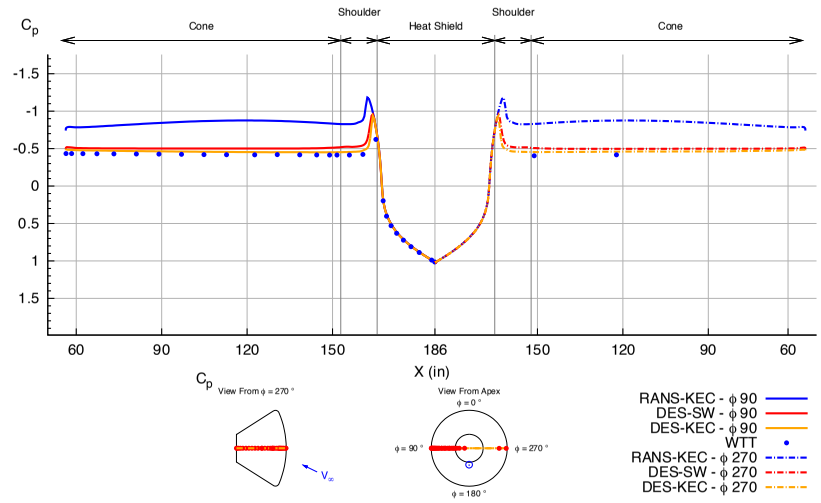

(b) $\phi = 90°$

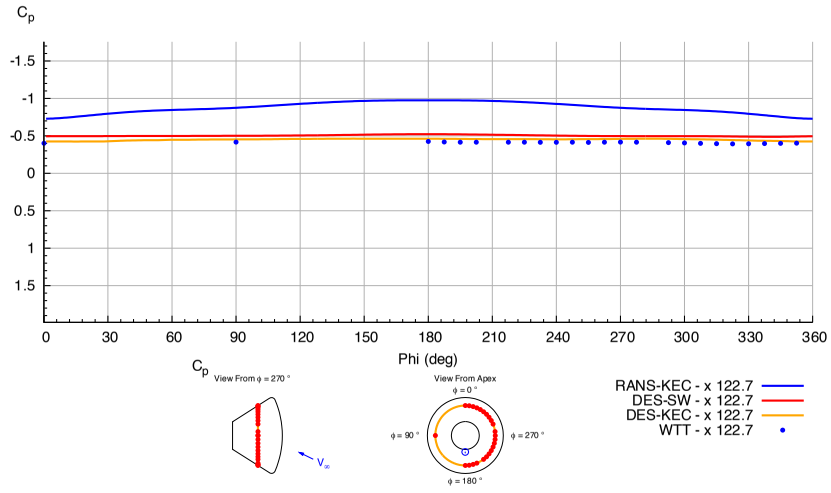

(c) X = 122.7”

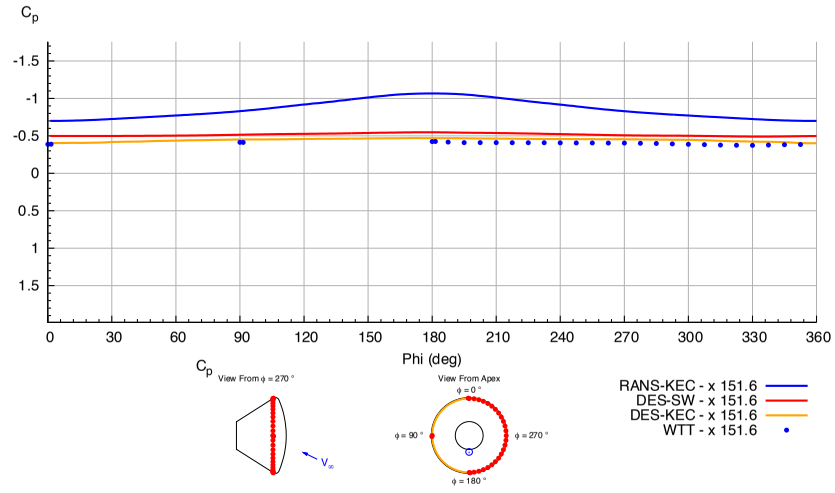

(d) X = 151.6”

Figure 27. Line plots of pressure tap data for Mach 0.95, $\alpha = 155°$ cases at various cuts along the fullscale geometry.

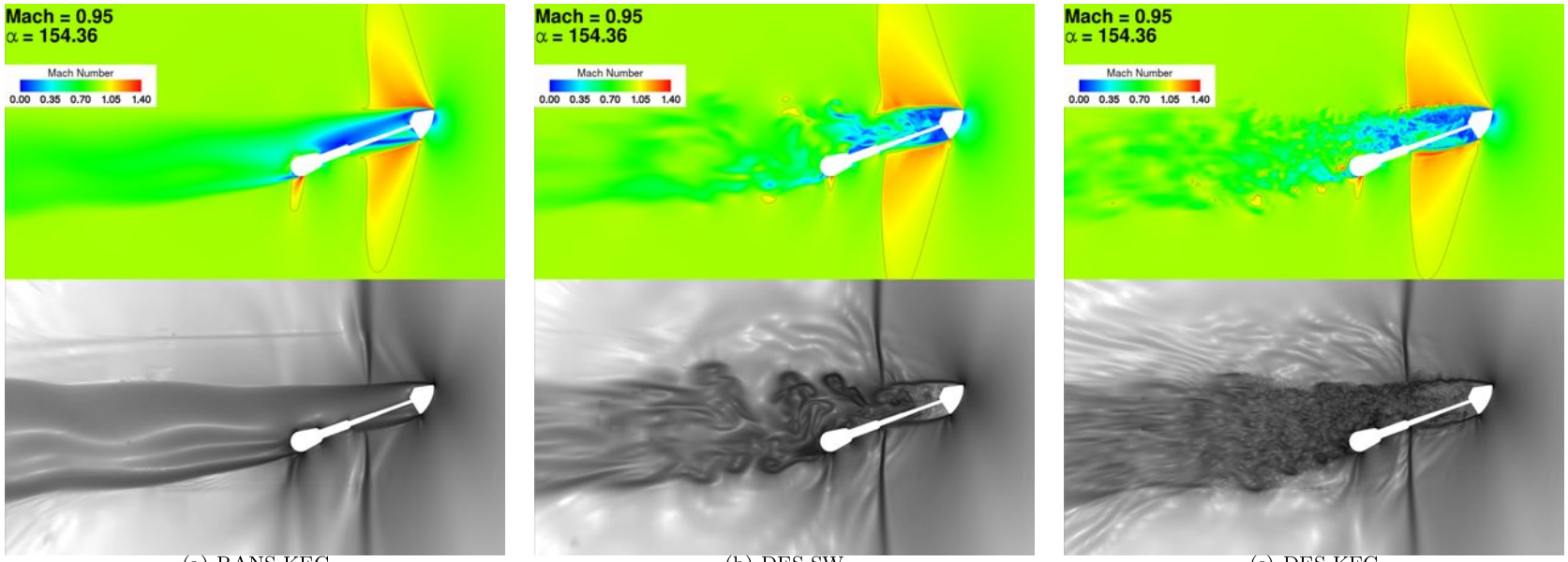

(a) RANS-KEC (b) DES-SW (c) DES-KEC

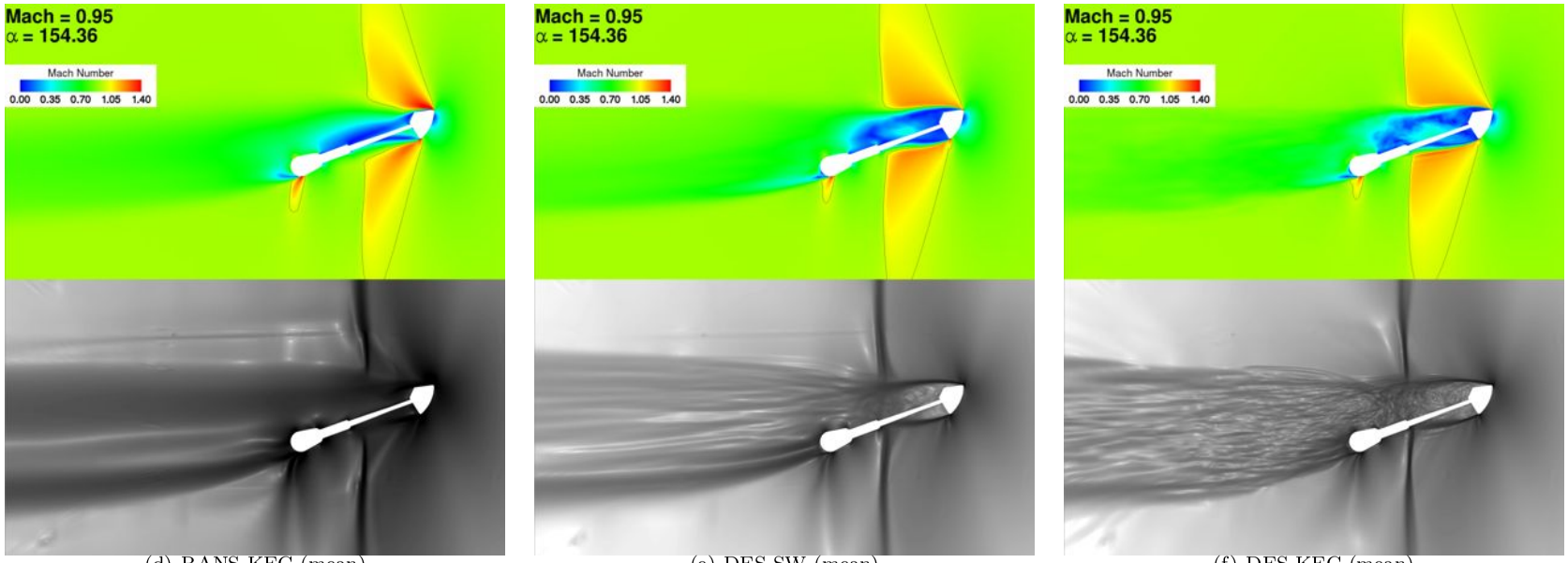

(d) RANS-KEC (mean) (e) DES-SW (mean) (f) DES-KEC (mean)

Figure 28. Plots of Mach number and log of density-gradient magnitude for both instantaneous and averaged cuts through the pitch plane (Y=0) at Mach 0.95, $\alpha = 155^\circ$.

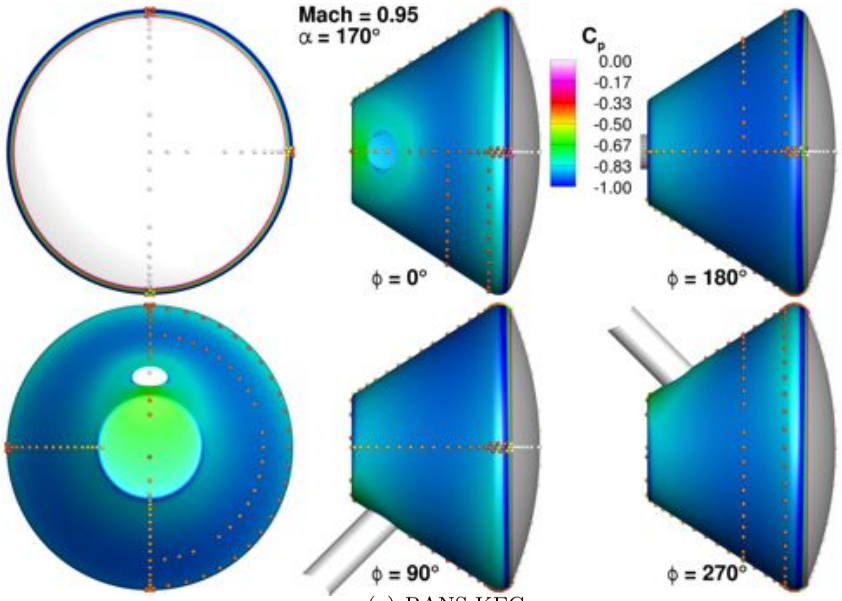

(a) RANS-KEC

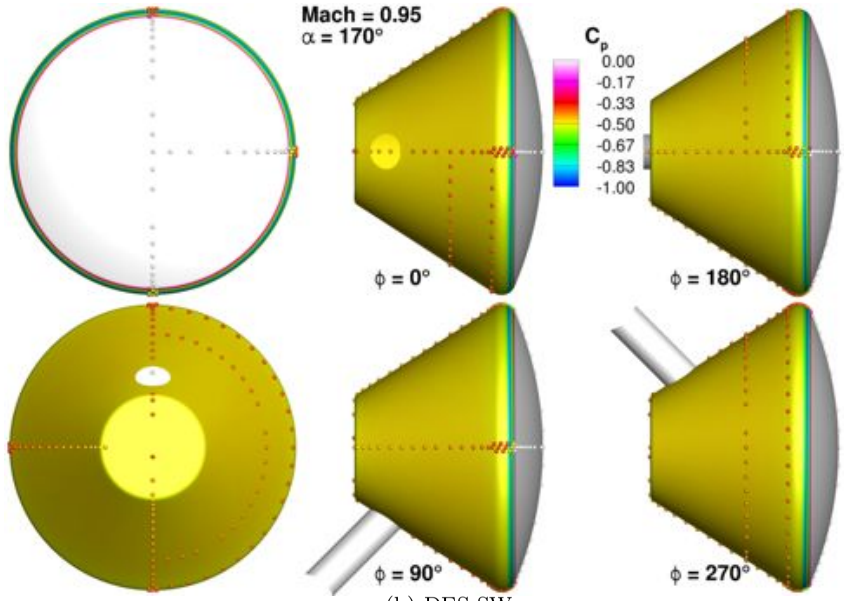

(b) DES-SW

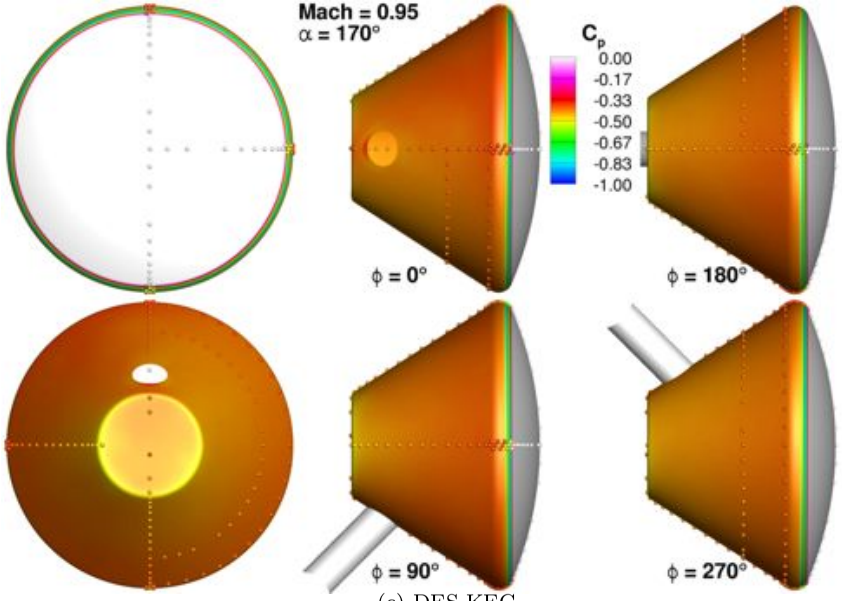

(c) DES-KEC

Figure 29. Freckle plots of pressure tap data for Mach 0.95, $\alpha = 170^\circ$ cases.

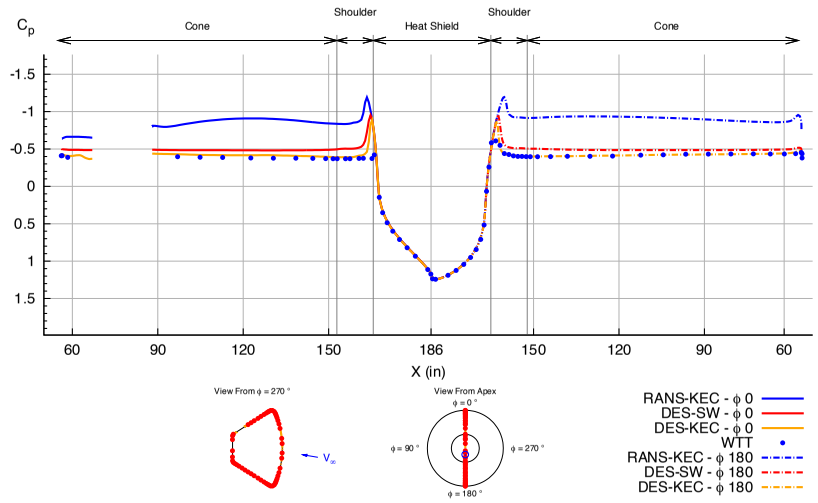

(a) $\phi = 0°$

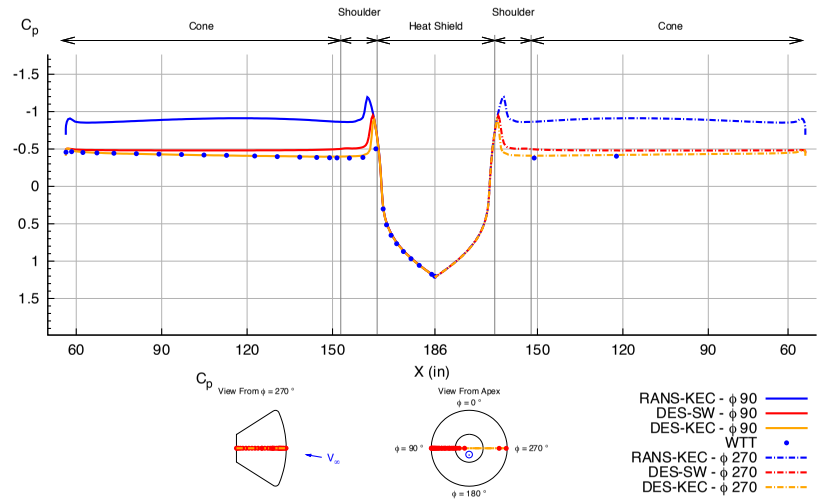

(b) $\phi = 90°$

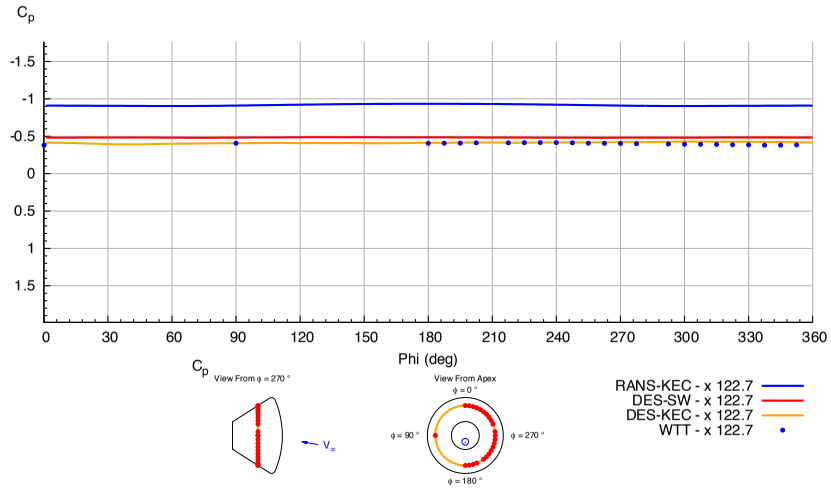

(c) X = 122.7”

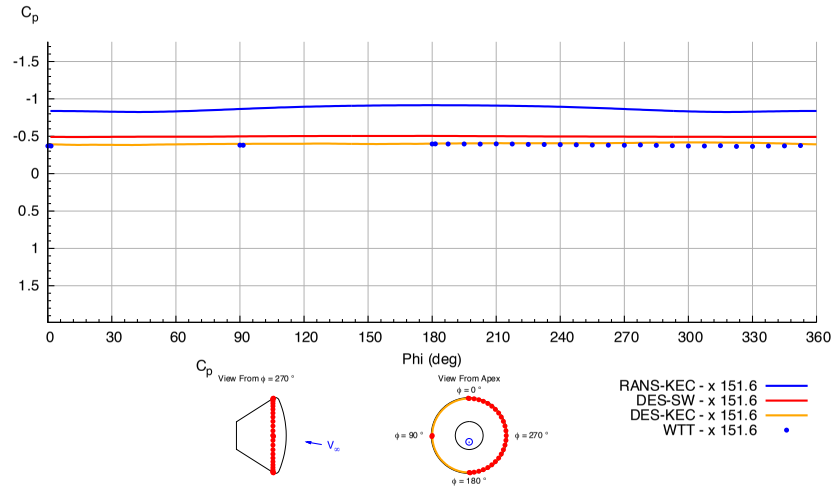

(d) X = 151.6”

Figure 30. Line plots of pressure tap data for Mach 0.95, $\alpha = 170°$ cases at various cuts along the fullscale geometry.

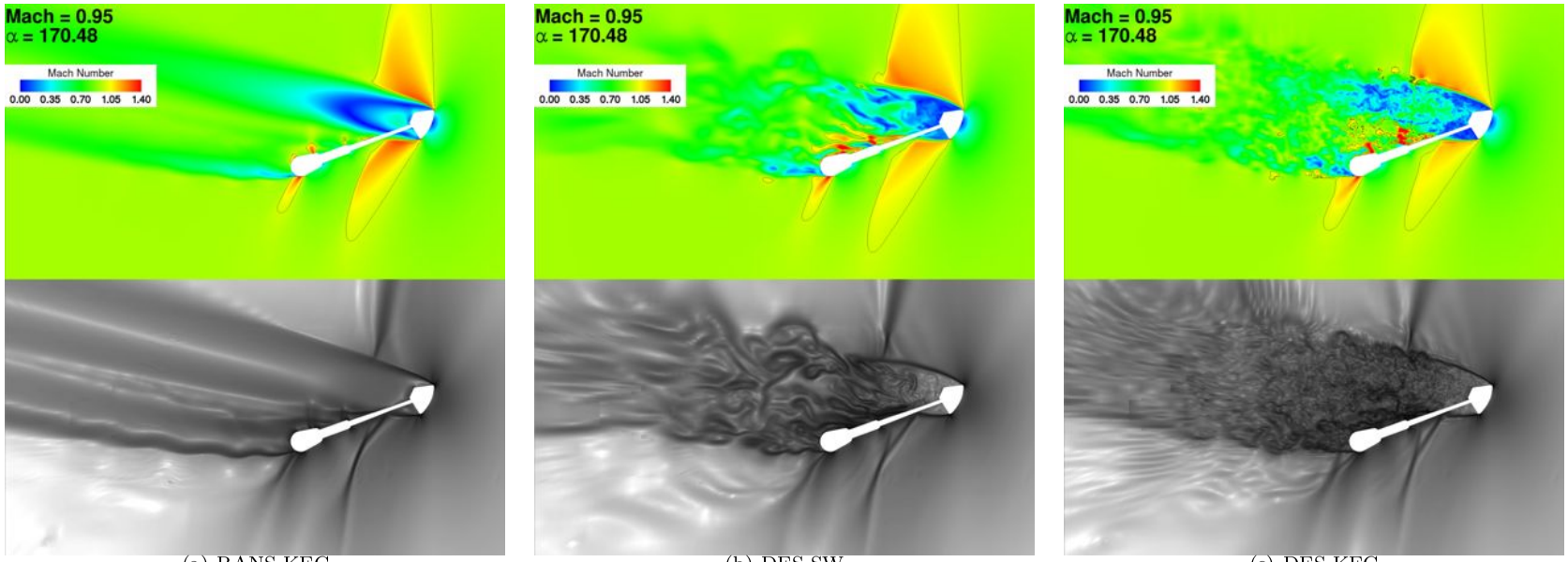

(a) RANS-KEC (b) DES-SW (c) DES-KEC

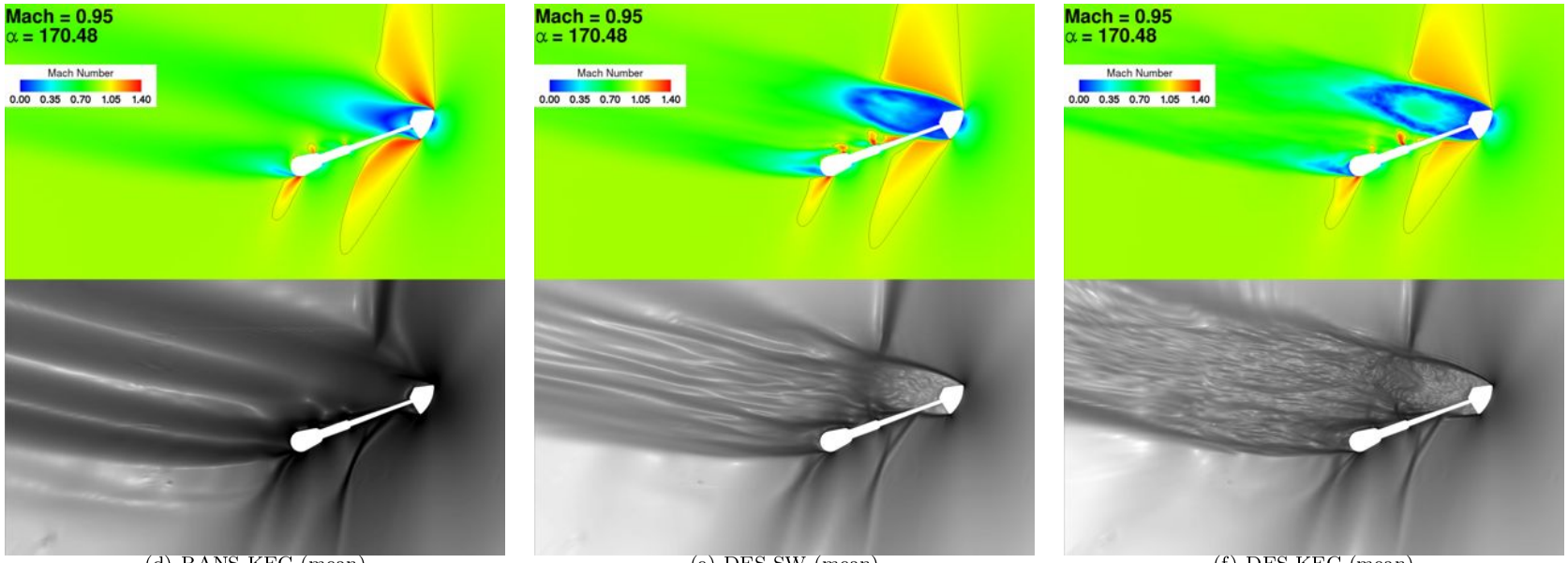

(d) RANS-KEC (mean) (e) DES-SW (mean) (f) DES-KEC (mean)

Figure 31. Plots of Mach number and log of density-gradient magnitude for both instantaneous and averaged cuts through the pitch plane (Y=0) at Mach 0.95, $\alpha = 170^\circ$.

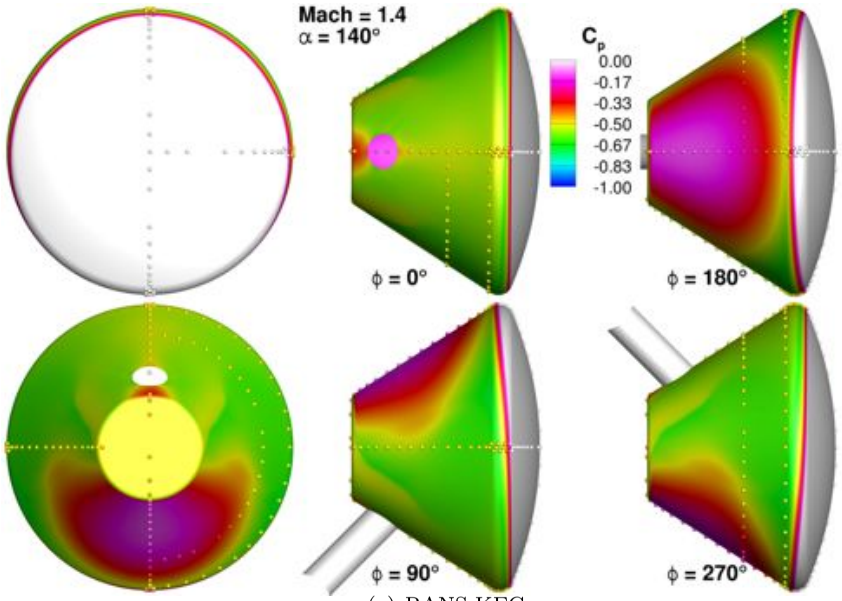

(a) RANS-KEC

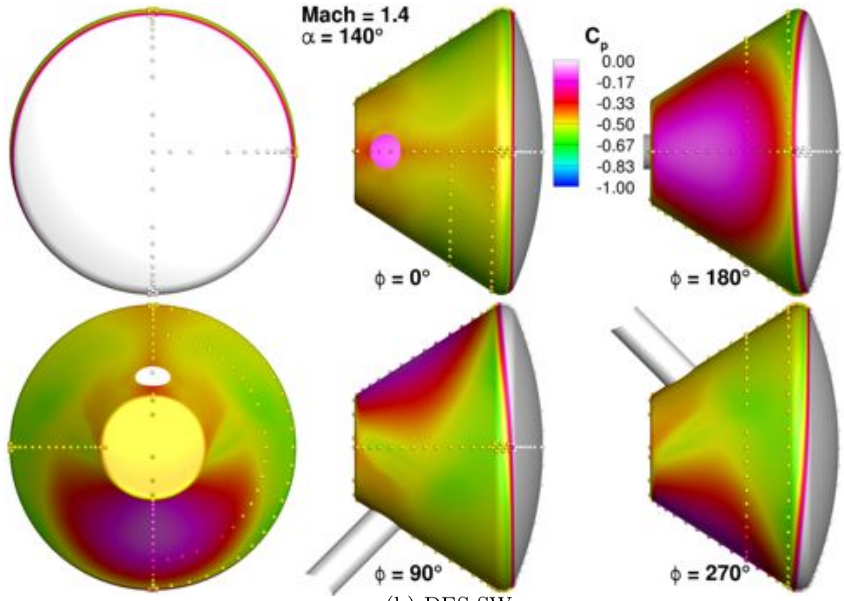

(b) DES-SW

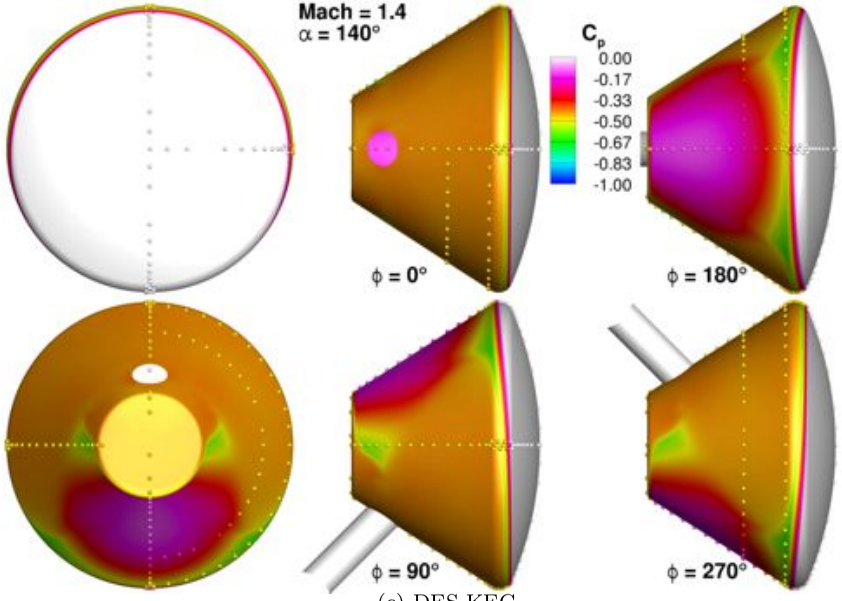

(c) DES-KEC

Figure 32. Freckle plots of pressure tap data for Mach 1.40, $\alpha = 140^\circ$ cases.

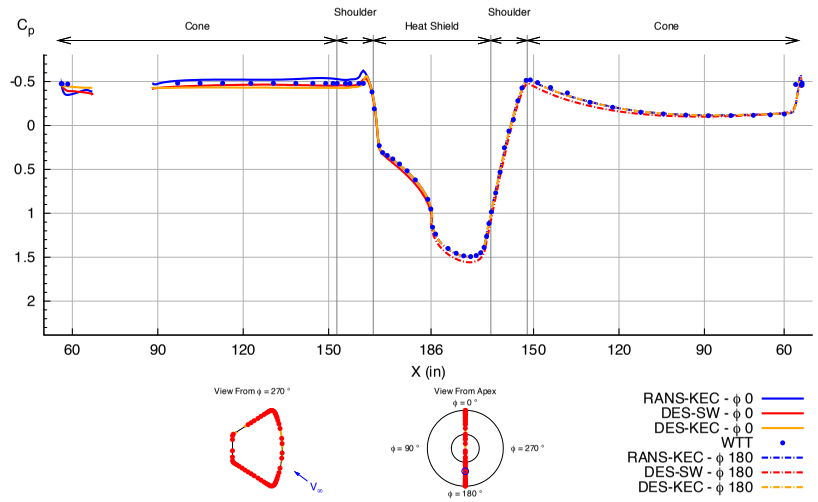

(a) $\phi = 0°$

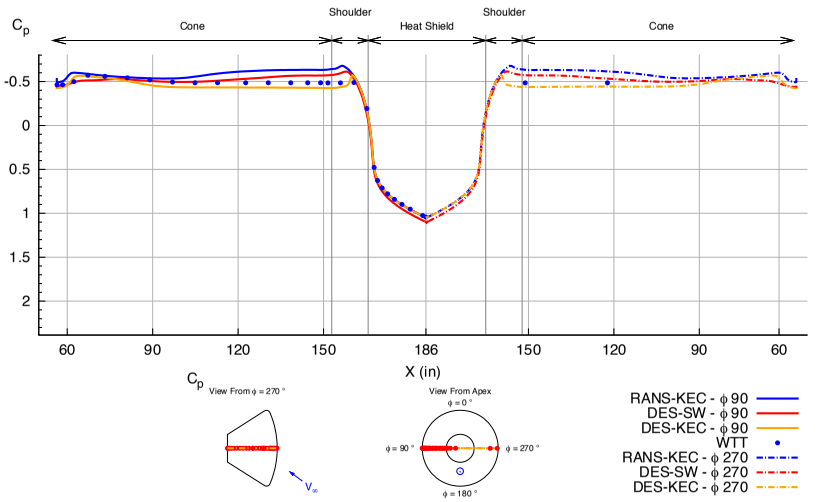

(b) $\phi = 90°$

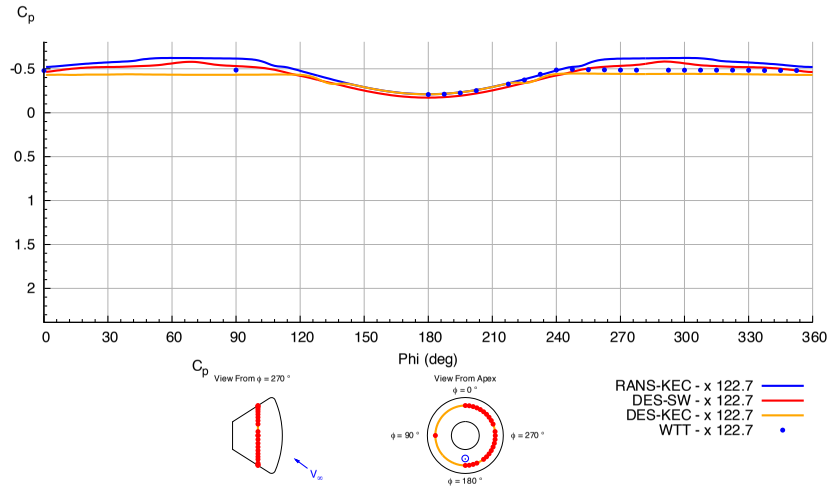

(c) X = 122.7”

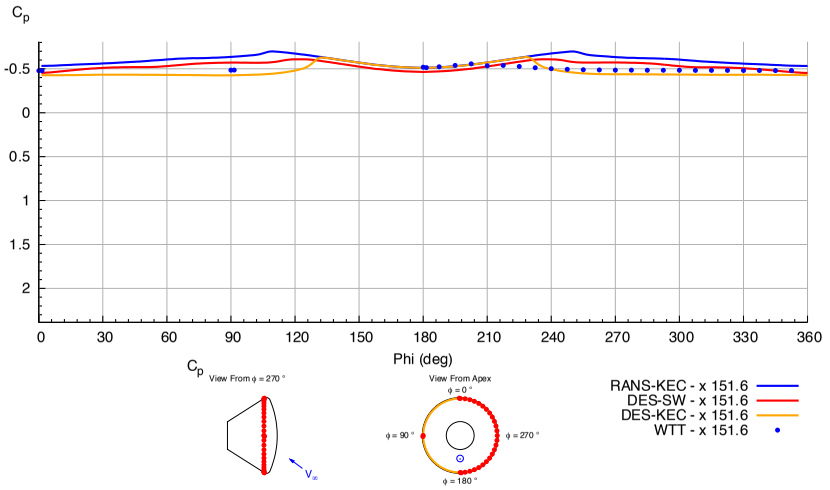

(d) X = 151.6”

Figure 33. Line plots of pressure tap data for Mach 1.40, $\alpha = 140°$ cases at various cuts along the fullscale geometry.

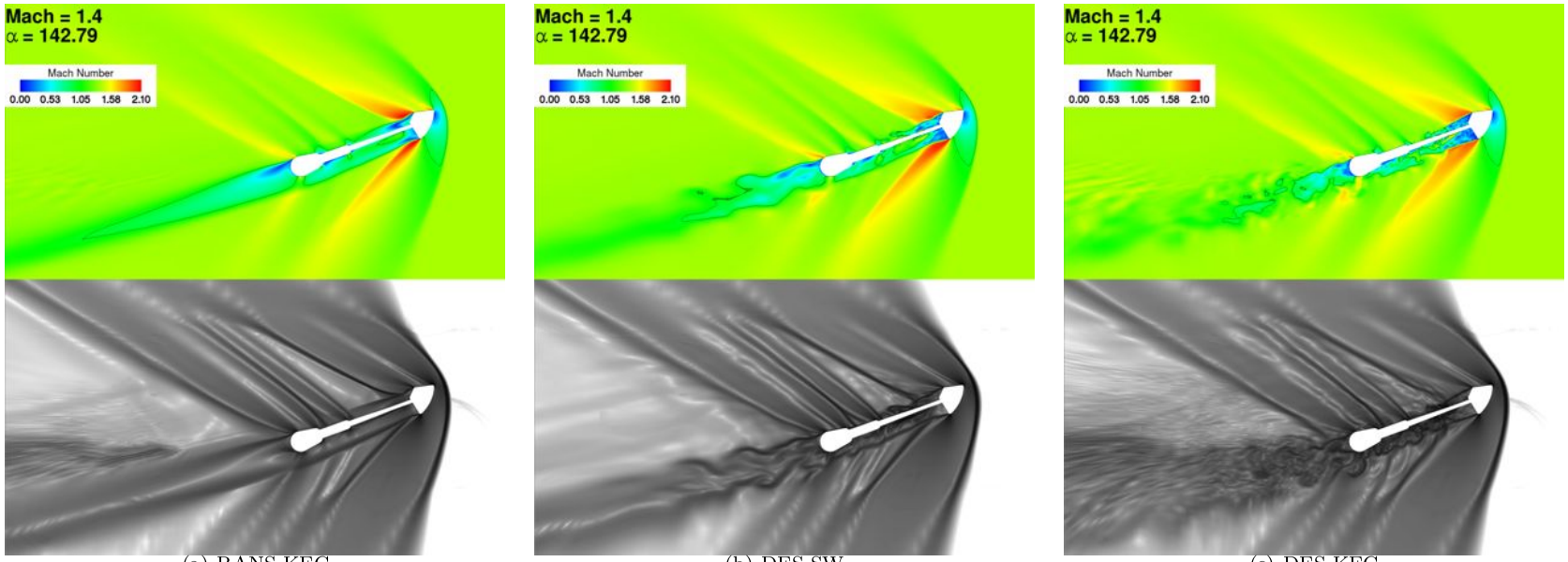

(a) RANS-KEC (b) DES-SW (c) DES-KEC

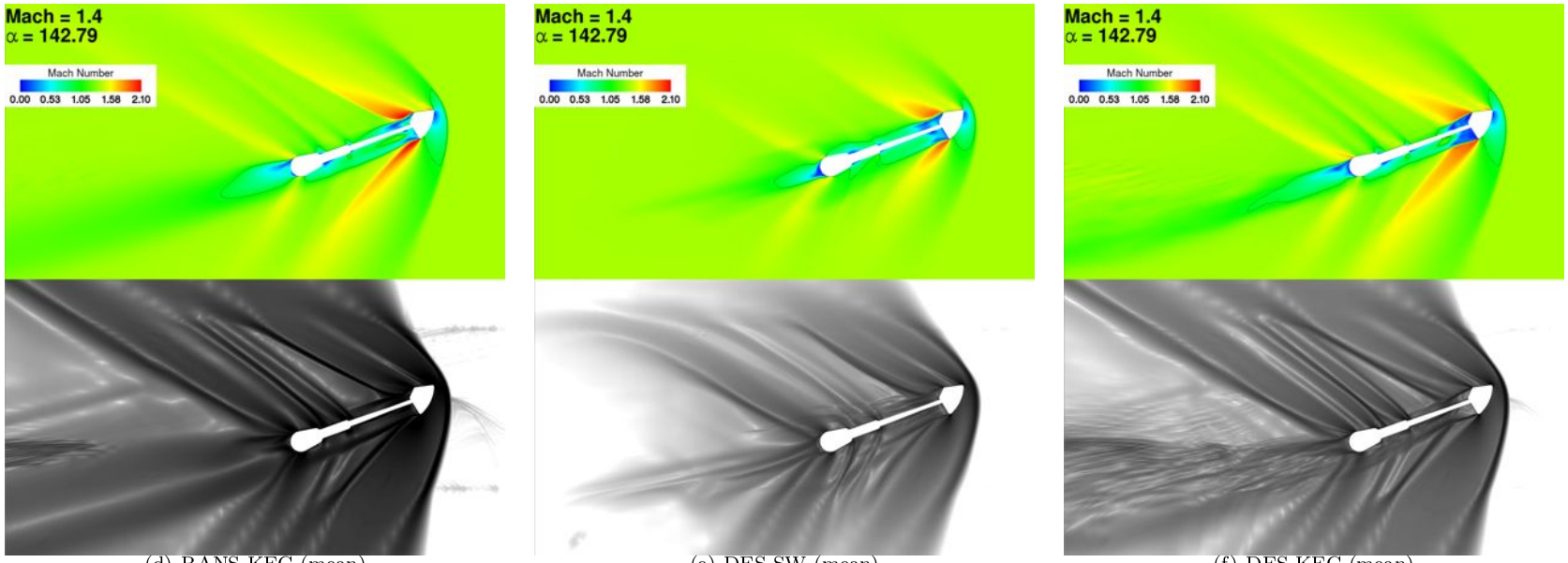

(d) RANS-KEC (mean) (e) DES-SW (mean) (f) DES-KEC (mean)

Figure 34. Plots of Mach number and log of density-gradient magnitude for both instantaneous and averaged cuts through the pitch plane (Y=0) at Mach 1.40, $\alpha = 140^\circ$.

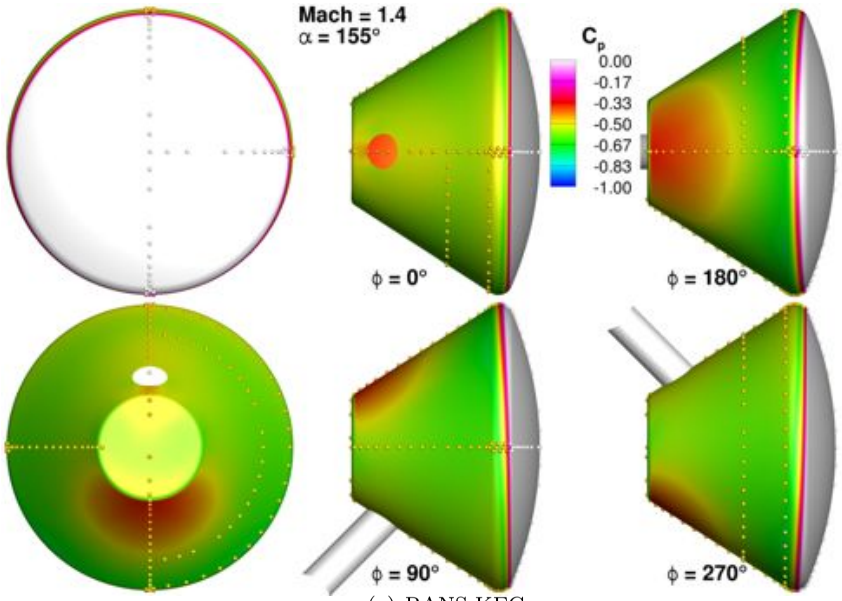

(a) RANS-KEC

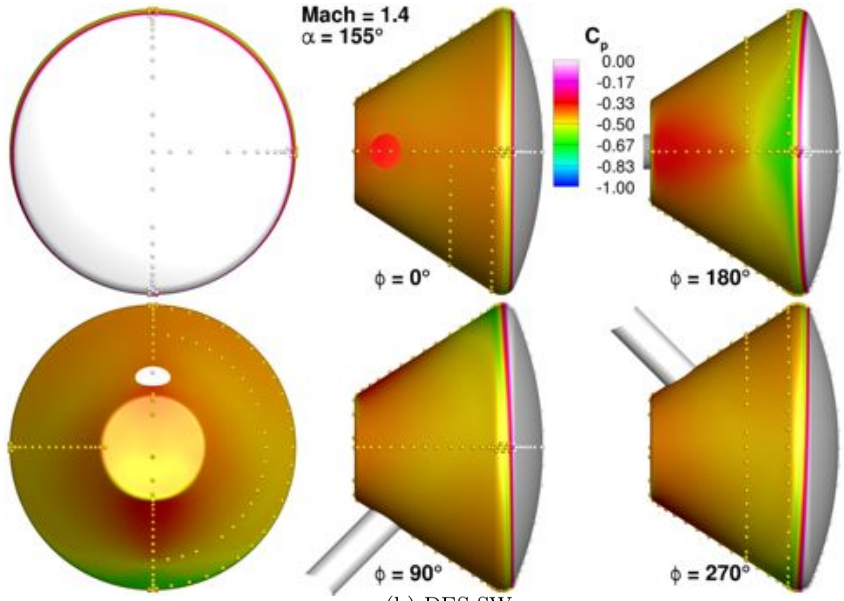

(b) DES-SW

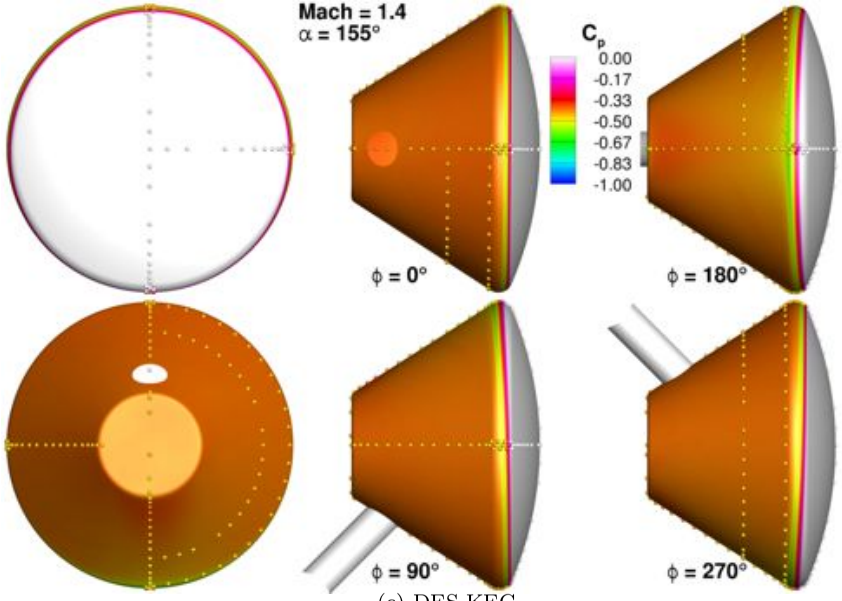

(c) DES-KEC

Figure 35. Freckle plots of pressure tap data for Mach 1.40, $\alpha = 155°$ cases.

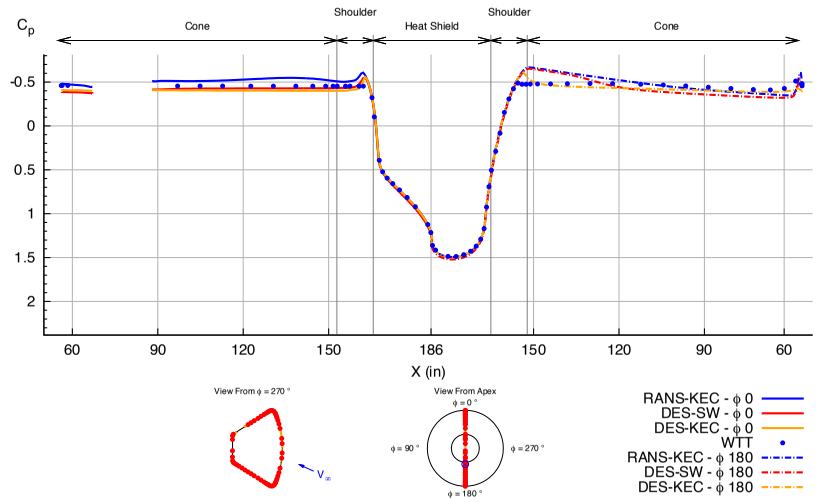

(a) $\phi = 0°$

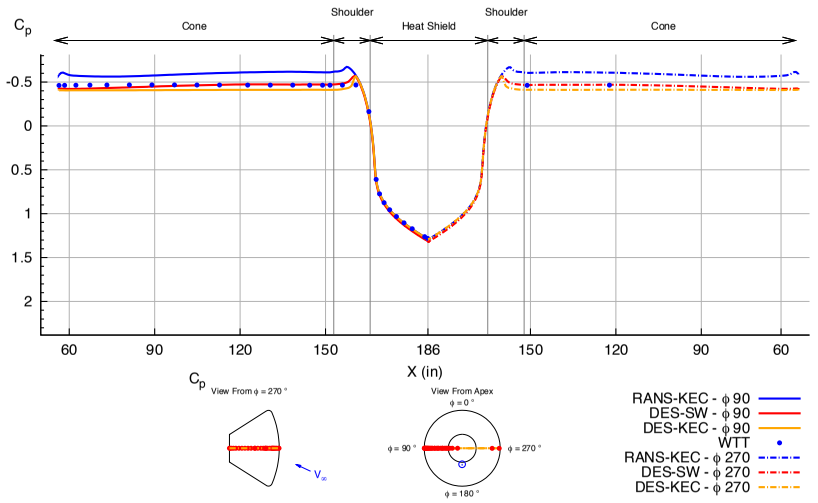

(b) $\phi = 90°$

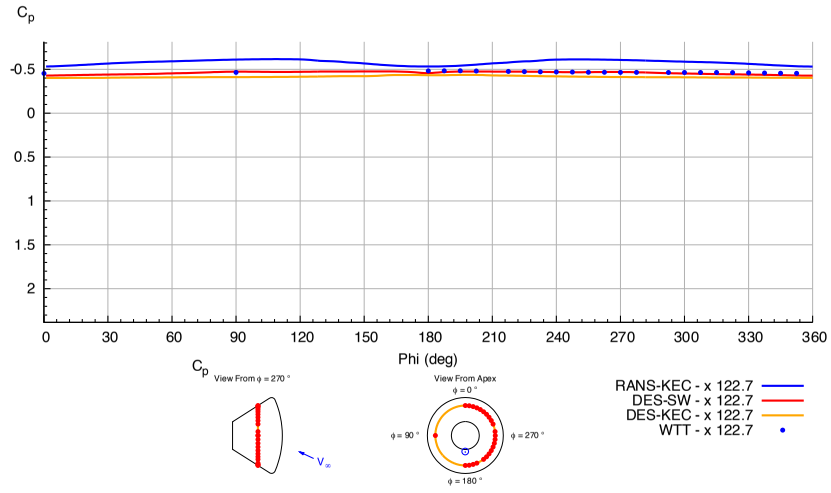

(c) X = 122.7”

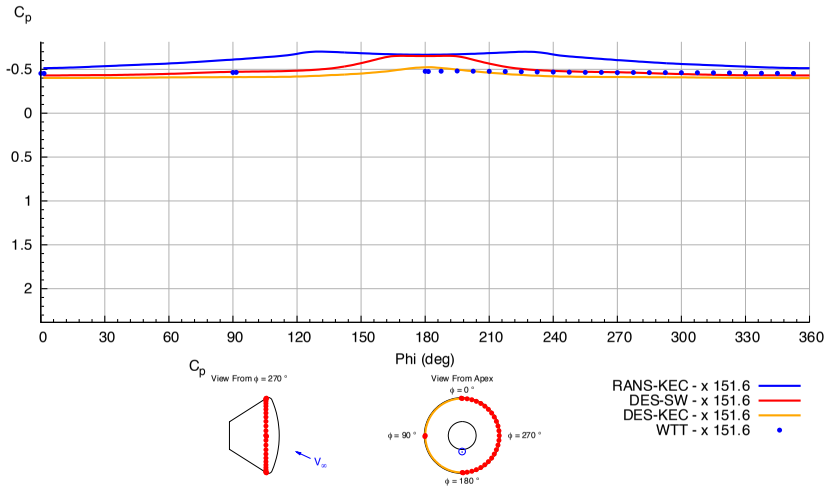

(d) X = 151.6”

Figure 36. Line plots of pressure tap data for Mach 1.40, $\alpha = 155°$ cases at various cuts along the fullscale geometry.

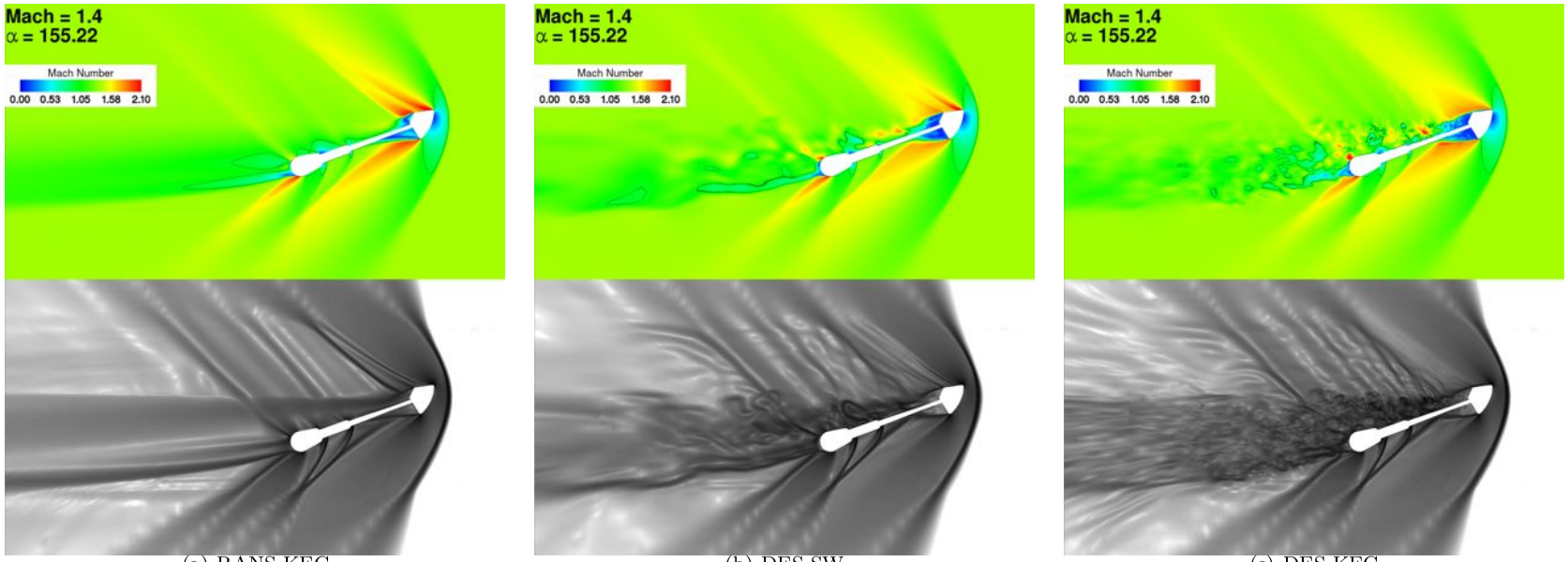

(a) RANS-KEC (b) DES-SW (c) DES-KEC

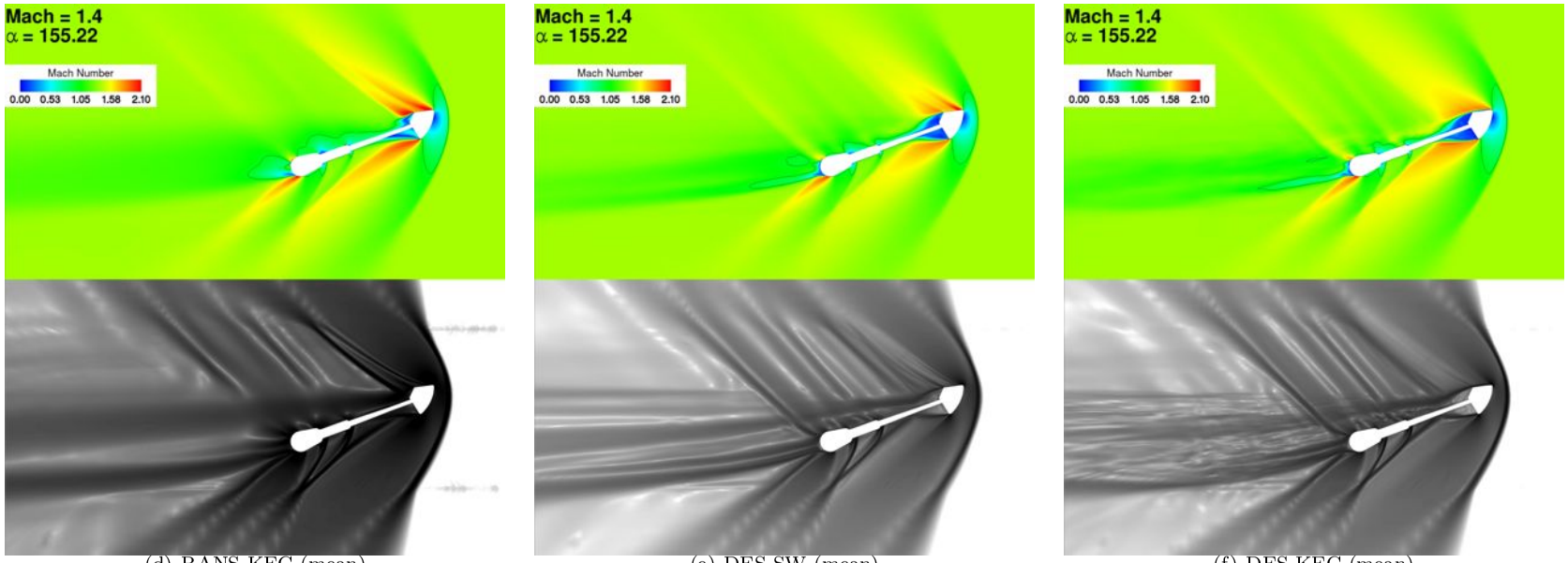

(d) RANS-KEC (mean) (e) DES-SW (mean) (f) DES-KEC (mean)

Figure 37. Plots of Mach number and log of density-gradient magnitude for both instantaneous and averaged cuts through the pitch plane (Y=0) at Mach 1.40, $\alpha = 155^\circ$.

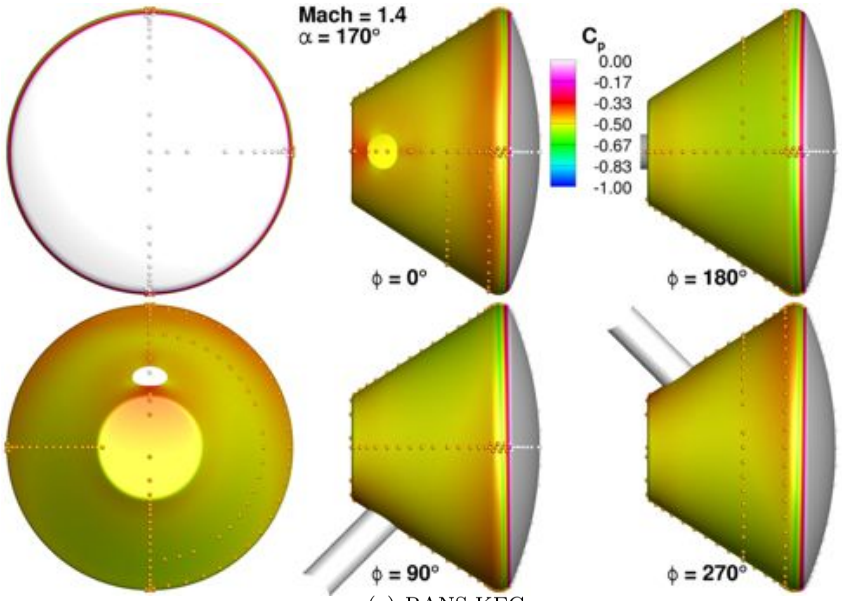

(a) RANS-KEC

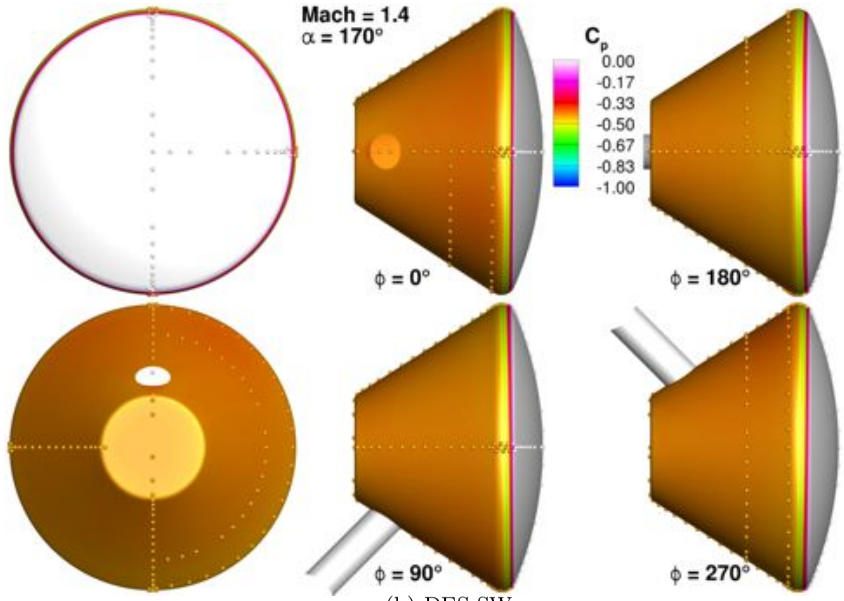

(b) DES-SW

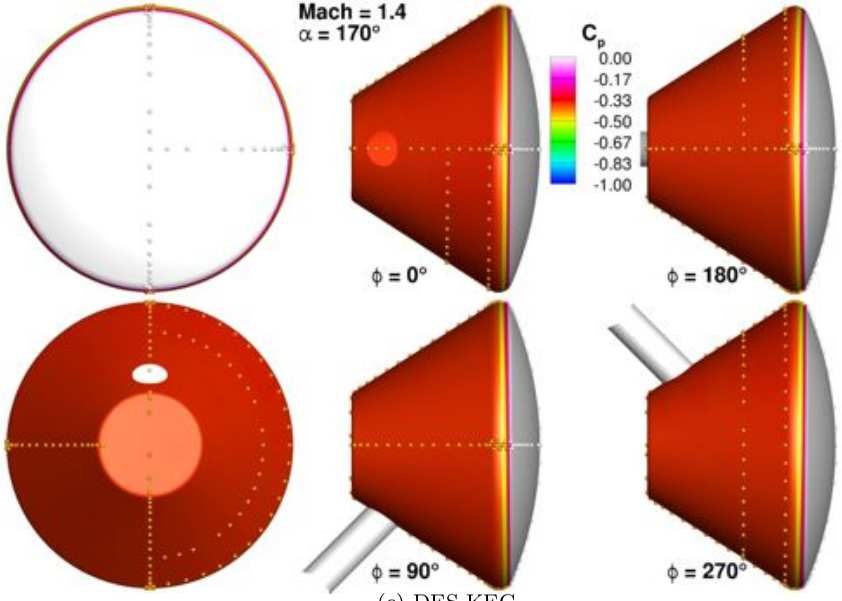

(c) DES-KEC

Figure 38. Freckle plots of pressure tap data for Mach 1.40, $\alpha = 170^\circ$ cases.

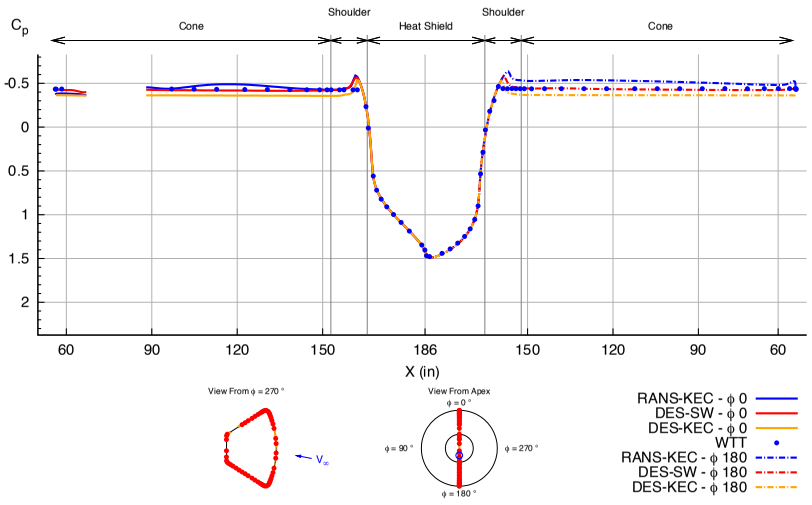

(a) $\phi = 0°$

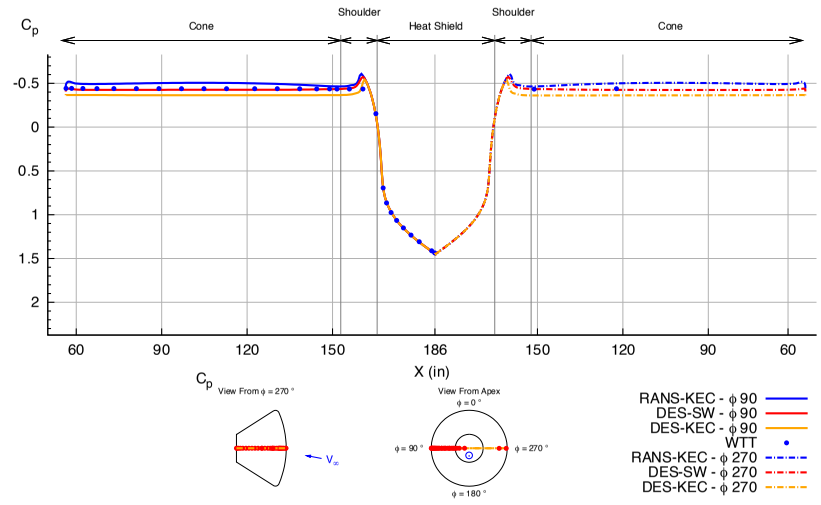

(b) $\phi = 90°$

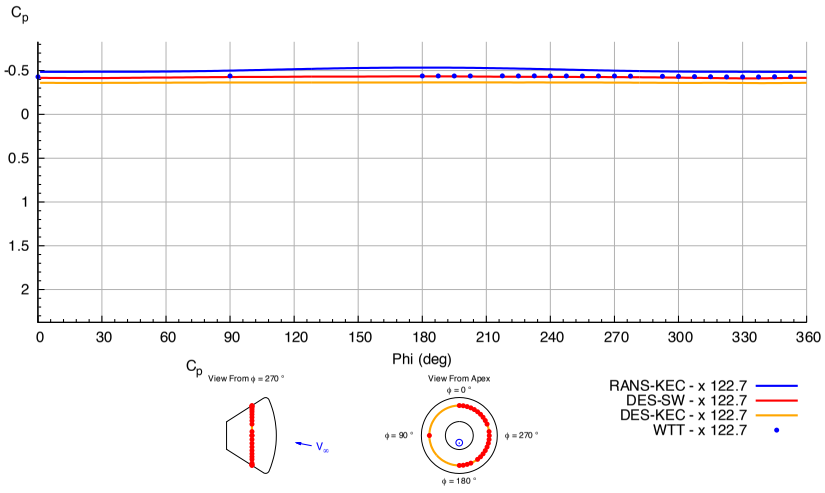

(c) X = 122.7”

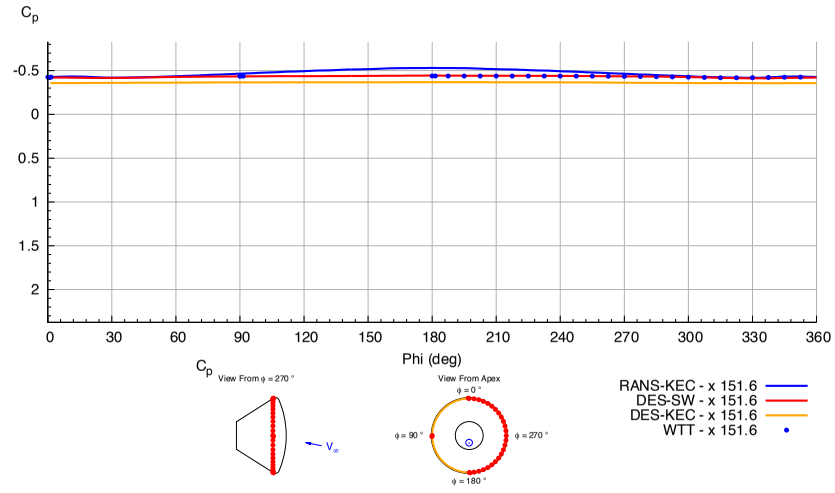

(d) X = 151.6”

Figure 39. Line plots of pressure tap data for Mach 1.40, $\alpha = 170°$ cases at various cuts along the fullscale geometry.

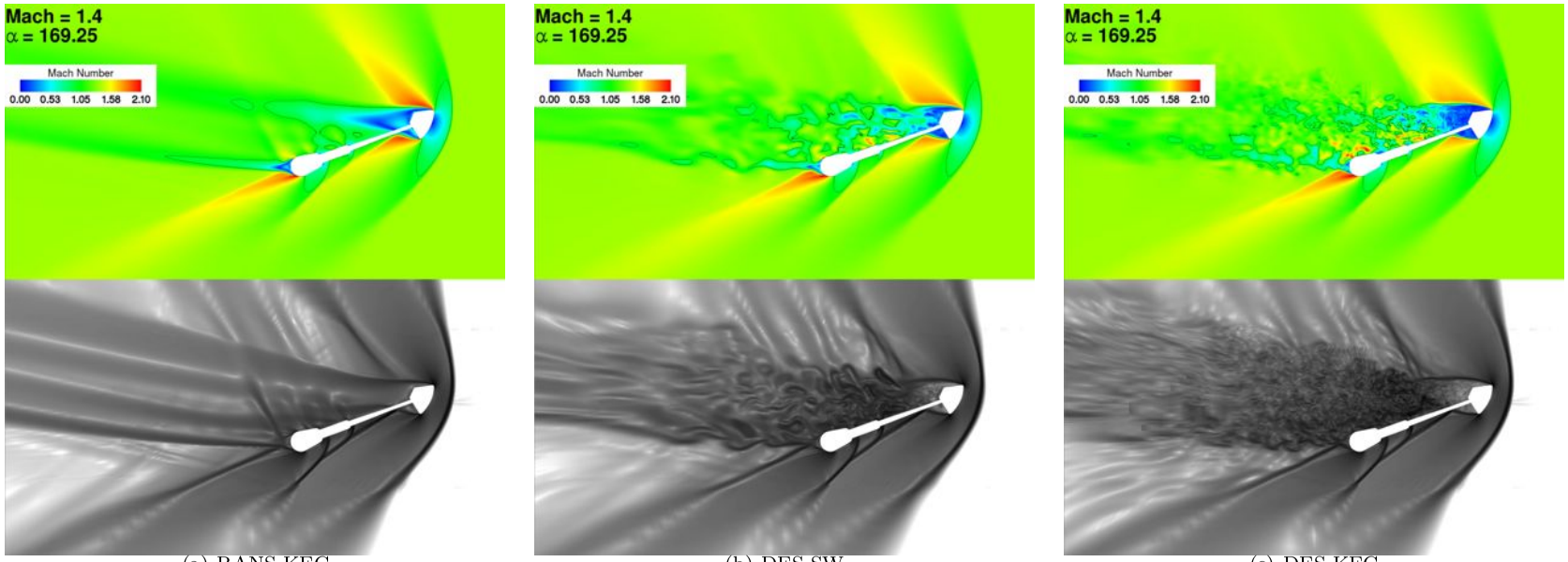

(a) RANS-KEC (b) DES-SW (c) DES-KEC

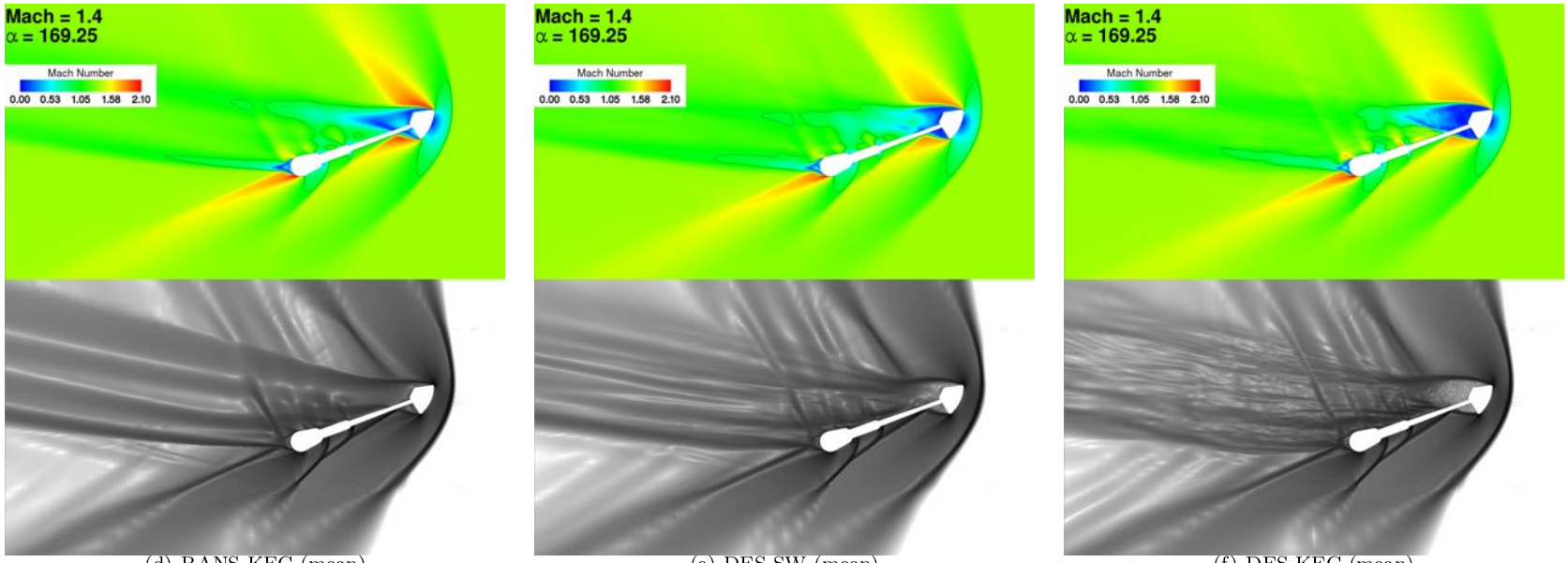

(d) RANS-KEC (mean) (e) DES-SW (mean) (f) DES-KEC (mean)

Figure 40. Plots of Mach number and log of density-gradient magnitude for both instantaneous and averaged cuts through the pitch plane (Y=0) at Mach 1.40, $\alpha = 170^\circ$.